Post-Inhibitory Rebound Spikes in Rat Medial Entorhinal Layer II/III Principal Cells: In-Vivo, In-Vitro, and Computational Modeling Characterization

ARTICLE *in* CEREBRAL CORTEX · FEBRUARY 2016

Impact Factor: 8.67 · DOI: 10.1093/cercor/bhw058

5 AUTHORS, INCLUDING:

Michele Ferrante

Boston University

24 PUBLICATIONS **184** CITATIONS

SEE PROFILE

Christopher F Shay

Boston University

12 PUBLICATIONS **112** CITATIONS

SEE PROFILE

Yusuke Tsuno

University of Utah

10 PUBLICATIONS **81** CITATIONS

SEE PROFILE

William George Chapman

Boston University

19 PUBLICATIONS **16** CITATIONS

SEE PROFILE

OXFORD UNIVERSITY PRESS | Cerebral Cortex

Post-Inhibitory Rebound Spikes in Rat Medial Entorhinal Layer II/III Principal Cells: *In-Vivo*, *In-Vitro*, and Computational Modeling Characterization

Journal:	*Cerebral Cortex*
Manuscript ID	CerCor-2015-00634.R2
Manuscript Type:	Original Articles
Date Submitted by the Author:	07-Feb-2016
Complete List of Authors:	Ferrante, Michele; Boston University, Dept. of Psychological and Brain Sciences Shay, CHRISTOPHER; Boston University, Department of Psychological and Brain Sciences Tsuno, YUSUKE; Boston University, Department of Psychological and Brain Sciences Chapman, G. William; Boston University, Boston University, Center for Systems Neuroscience, Center for Memory and Brain, Department of Psychological and Brain Sciences, Graduate Program for Neuroscience Boston, Massachusetts, United States Hasselmo, Michael; Boston University, Psychology
Keywords:	Stellate Cells, Entorhinal Cortex, Hyperpolarization-activated cation current (Ih), Inhibition, Post-Inhibitory Action Potentials

Title: Post-Inhibitory Rebound Spikes in Rat Medial Entorhinal Layer II/III Principal Cells: *In-Vivo*, *In-Vitro*, and Computational Modeling Characterization

Running Title: Post-inhibitory Spikes in Medial Entorhinal

MICHELE FERRANTE,[1,2] CHRISTOPHER F SHAY,[1,2,3] YUSUKE TSUNO,[1,2] G WILLIAM CHAPMAN[1], and MICHAEL E HASSELMO[1,2,3]

[1] Center for Memory and Brain, Boston University, Boston, MA, 02215
[2] Department of Psychological and Brain Sciences, Boston University, Boston, MA, 02215
[3] Graduate Program for Neuroscience (GPN), Boston University, Boston, MA, 02215

Correspondence: Michele Ferrante, 2 Cummington Mall, Boston 02215, MA. Ph. 339-223-2340, mferr133@bu.edu

Abstract

Medial Entorhinal Cortex Layer-II stellate cells (mEC-LII-SCs) primarily interact via inhibitory interneurons. This suggests the presence of alternative mechanisms other than excitatory synaptic inputs for triggering action potentials (APs) in stellate cells during spatial navigation. Our intracellular recordings show that the hyperpolarization-activated cation current (I_h) allows Post-Inhibitory-Rebound-Spikes (PIRS) in mEC-LII-SCs. *In-vivo,* strong Inhibitory-Post-Synaptic-Potentials (IPSPs) immediately preceded most APs shortening their delay and enhancing excitability. *In-vitro* experiments showed that inhibition initiated spikes more effectively than excitation and that more dorsal mEC-LII-SCs produced faster and more synchronous spikes. In contrast, PIRS in Layer-II/III pyramidal cells (PCs) were harder to evoke, voltage-independent, and slower in dorsal mEC. In computational simulations, mEC-LII-SCs morphology and I_h homeostatically regulated the dorso-ventral (DV) differences in PIRS timing and most dendrites generated PIRS with a narrow range of stimulus amplitudes. These results suggest inhibitory inputs could mediate the emergence of grid cell firing in a neuronal network.

Keywords: stellate cells, inhibition, entorhinal cortex, hyperpolarization-activated cation current (I_h), post-inhibitory spikes

INTRODUCTION

As a rat navigates its environment, grid cells in the medial entorhinal cortex (mEC) spike in a regular array of locations corresponding to the vertices of triangles tessellating the explored space (Fyhn et al., 2004; Hafting et al., 2005; Moser and Moser, 2008). The size of triangles correlates with the location of the grid cell along the dorsal to ventral axis of the mEC (Hafting et al., 2005; Brun et al., 2008) and it is believed to be a mechanism used by the animal to scale space. The mEC thus transforms sensory inputs from the environment into durable allocentric representations that could be used for path integration (Fyhn et al., 2004). Intracellular recordings from mEC layer-II stellate cells (mEC-LII-SCs) and layer-II/III pyramidal cells (mEC-LII/III-PCs) during spatial navigation showed that these cells exhibit grid cell firing properties (Domnisoru et al., 2013; Schmidt-Hieber and Häusser, 2013). Spatio-temporal computations performed in mEC most likely involve synaptic interactions between mEC-LII-SCs and local inhibitory interneurons (Pastoll et al., 2013; Couey et al., 2013). Recent data suggests that mEC-LII-SCs are indirectly connected mostly through inhibitory interneurons and that synaptic inhibition in mEC-LII-SCs is substantially stronger than excitation (Pastoll et al., 2013; Beed et al., 2013; Couey et al., 2013). Furthermore, the remarkable diversity in the morphological and intrinsic properties of entorhinal cortex interneurons (Ferrante et al., 2015) may underlie their complex role in orchestrating spatial memory functions by this brain region.

GABAergic interneurons are classically thought to prevent post-synaptic cell firing (Miles et al., 1996; Jahnsen and Llinas 1984; McCormick 1998; McCormick and Bal 1997; Person and Perkel 2005), synchronize oscillations (Buzsaki 2002; Buzsaki and Draguhn 2004; Steriade et al., 1993) or buffer a steep neuronal input-output frequency relationship (Ferrante et al., 2009). Nevertheless, target cell rebound spikes may be elicited in response to inhibitory signals (Jahnsen and Llinas 1984; McCormick and Bal 1997; McCormick 1998) and a mechanistic explanation of grid cell firing could involve Post-Inhibitory Rebound Spikes (PIRS) (Hasselmo, 2013). Hence, a post-inhibitory rebound is a period of intrinsically generated neuronal excitability following the termination of inhibition. PIRS have been recorded *in-vitro* in mEC-LII-SCs (Alonso and Llinas, 1989; Alonso and Klink, 1993; Dickson et al., 2000; Giocomo et al., 2007; Heys et al., 2010) but the intrinsic and extrinsic properties modulating the emergence of PIRS have not been systematically analyzed before the present study, particularly, with respect to the cellular position along the mEC dorsal-ventral axis.

PIRS have also been recorded *in-vivo,* for instance between putatively connected entorhinal interneurons using extracellular recording (Adhikari et al., 2012); or in a subset of offset neurons in the inferior colliculus that fire at the termination of sounds (Kasai et al., 2012); or in deep cerebellar nuclear neurons when the incoming inhibitory inputs from Purkinje cells get synchronously activated by climbing fibers (Bengtsson et al., 2011). Before our study, similar *in-vivo* intracellular analyses of PIRS have not been performed in mECLII-SCs. Functionally PIRS in mEC grid cells, like in the olfactory bulb (Isaacson and Strowbridge 1998; Yokoi et al., 1995), may sharpen the spatial pattern of activity. Or, perhaps like in subcortical regions (Bottjer, 2005), PIRS may regulate persistent firing and rhythms. One of the reasons why only few examples of PIRS have been observed *in-vivo* is that the specific neuronal connectivity responsible for them may be activity- and/or cell-dependent (Adhikari et al., 2012).

Membrane potential dynamics and intrinsic properties are responsible for the emergence of PIRS, including the effects of the I_h current that responds to hyperpolarization by generating a depolarizing current that slowly turns on and off. When the hyperpolarization generated by the activation of inhibitory synapses decays, the slow offset of the I_h current results in a depolarizing current that lasts longer than the inhibition, giving rise to the characteristic depolarizing overshoot, and providing a mechanism for generating APs. Intuitively, PIRS in mEC neurons should emerge from the synergistic interaction of strong/frequent inhibitory inputs and large I_h conductances. This is because being hyperpolarization-activated, I_h, creates larger depolarizing rebound potentials when stronger (or temporally clustered) inhibitory synaptic inputs interact with larger I_h conductances.. mEC-LII-SCs express large amounts of I_h

(Alonso and Llinas, 1989; Klink and Alonso, 1993; Leung and Yu, 1998; Heys and Hasselmo, 2012; Shay et al., 2012) that coupled with large-amplitude IPSPs (Cunningham et al., 2003) may generate PIRS. Additionally, these strong IPSPs from local PV+ interneurons arrive at a fast (gamma) pace (Cunningham et al., 2003) potentially enabling more temporal summation that might lead to an enhanced probability to generate PIRS. In particular, cortical gamma oscillations are thought to enable associative binding while processing incoming sensory signals (Gray et al., 1989; Singer and Gray, 1995; Verala et al., 2001). The frequency of incoming IPSPs from PV+ cells decreases at more ventral positions in mEC (Beed et al., 2013), suggesting that this could be a mechanism enabling the emergence of the larger grid cell firing fields observed in the ventral mEC. Furthermore, IPSPs from PV+ cells may provide recurrent mEC inhibition driven by grid cells (Buetfering et al., 2014) therefore silencing non-grid cells and enabling PIRS in nearby cells expressing I_h.

Countless neuronal functions depend on fine details of complex molecular, circuit, and synaptic architectures that occur between and within cells. Until recently (Micheva and Smith, 2007), with the advent of array tomography, simultaneously investigating these three levels, even in a single cell (at the nanometer scale) was not possible and it still represents a technological challenge. Specifically, the spatial distribution of ionic channels synapses on dendrites of mEC-LII-SCs remains unknown, but knowledge of this could perhaps help us answer important questions. Such as, how peri-somatically initiated PIRS backpropagate into the dendrites and how active and passive properties affect this propagation. Somatic recordings of synaptically stimulated dendrites showed the co-activation of inward (*i.e.,* I_{Nap} and I_{CaT} (Magee and Johnston, 1995)) and outward (*i.e.,* I_{KA} (Hoffman et al., 1997)) active properties which in turn can shaped unitary AMPA and NMDA EPSP currents (Perez-Rosello et al., 2011). Unfortunately, a similar investigation for GABA(/hyperpolarization)-activated conductances has not been carried out in mEC-LII-SCs. The ability to generate a rebound spike maybe influenced by the spatial distribution of synapses that is highly cell specific (Gulyas et al., 1999), or by the amplitude of the synaptic potentials that may vary with distance from the soma (Magee and Cook, 2000).

The cellular properties of mEC-LII-SCs may be specifically tuned to allow them to easily generate PIRS and this could be an important biophysical mechanism enabling the neural substrate to encode spatial navigation in the mEC. Furthermore, neuropharmacological enhancement of I_h can be achieved by administering the anticonvulsant lamotrigine (Poolos et al., 2002; Ferrante et al., 2008) while its down-regulation can be attained through the use of ZD 7288 (Harris and Constanti, 1995). The pharmacological and up- and down-regulation of I_h in grid cells can be an important target for future drugs aiming to treat diseases affecting spatial memory (*e.g.,* Alzheimer's Disease). Recent experiments and simulations have shown (Ascoli et al., 2010) that upon release from hyperpolarizing current step injections, I_{KA} blockage resulted in peri-somatic initiation of PIRS that could be blocked by ZD 7288. Therefore I_{KA} and I_h could counteract each other in promoting (or inhibiting) PIRS. Despite this extensive wealth of accumulated knowledge (mostly in other brain regions) we are still missing a quantitative description of how mEC-LII/III principal cells generate PIRS and what role they may play in the emergence and modulation of grid cell firing. This would include a comprehensive characterization of the stimuli and neuronal features enabling mEC-LII/III principal cells to generate spikes in response to inhibition.

MATERIALS AND METHODS

All experimental protocols were approved by the Boston University Institutional Care and Use Committee and The Animal Welfare Act. All experiments were conducted on male and female Long–Evans rats (Charles River Laboratories, Wilmington, MA, USA). Unless otherwise specified, significance (/p-value) and correlation coefficient (R) for the *in-vivo* and *in-vitro* results were calculated using the Pearson correlation coefficient (Wessa, 2012) and were noted in the respective figure legends.

***In-Vivo* Electrophysiology**

All the *in-vivo* data used for this study was from our previous investigations (Tsuno et al., 2013); more details on the methods used to collect these *in-vivo* data can be found in the original manuscript. Briefly, adult (250-400 gr) rats were used for these experiments. After the animals were anaesthetized a hole was drilled in the skull and a sharp intracellular recording glass electrode was lowered in the mEC (lateral 4.5 mm, 0.35–1.00 mm anterior from the sinus on the cerebellum, angled 12 degrees to anterior, depth 2.0–4.5 mm from the surface) by a micromanipulator (MO-8-W; Narishige). With this experimental setup current stimulations and voltage intracellular recordings were simultaneously performed. In some experiments, 1 mM picrotoxin (#1128; Tocris, Bristol, England, UK) was diluted in the internal solution of the recording electrode.

***In-vitro* Electrophysiology**

Brain slicing and recording techniques have been previously described (Shay et al., 2012) where more in depth methodological details can be found. Current-clamp, whole-cell recordings were performed at physiological temperature (36±2 °C) from the soma of LII-SCs and LII/III-PCs at different locations along the DV axis of the mEC.

17 to 21-day-old male rats were deeply anesthetized with (1.5ml) isoflurane (Abbot Laboratories) in diffusion chambers. After establishing the absence of tail and pedal reflex, brains were extracted and swiftly placed in ice-cold aCSF (125 NaCl, 2 CaCl, 2.5 KCl, 1.25 NaH2PO4, 25 NaHCO3, 25 D-Glucose, and 1 MgCl2, in mM) with pH of 7.4. Acute (400 µm-thick) horizontal parahippocampal slices were obtained using a vibrating blade microtome (Leica VT1000). Brain slices were incubated for 30 minutes in a holding chamber filled with aCSF at 31°C and for an additional 30 minutes at room temperature while being constantly bubbled with a mixture of 95% O2 - 5% CO2 during the whole experiment.

Recording pipettes were made from borosilicate glass capillaries using a P-90 horizontal puller (Sutter Instruments) and filled with intracellular recording solution containing the following concentrations (in mM): 110 K-gluconate, 20 KCl, 1 EGTA, 2 MgCl2, 10 HEPES, 2 Na2ATP, 0.3 Na2GTP, 10 phosphocreatine, and 0.1% biocytin (for postfix labeling). Filled pipettes had resistances of 4±1 MΩ. An upright microscope (Zeiss Axioskop 2 or Olympus BX51I) equipped with a 40× immersion lens and a near infrared charge-coupled device (CCD) camera (JAI CV-M50IR) or digital Rolera Bolt camera (QImaging, Surrey, BC, Canada) were used to visualize the cells.

After a strong (>1 GΩ) seal was achieved negative pressure was applied to the recording electrode to gain whole cell access, the cells were then allowed 3-5 min to recover. The delay of the spike and the number of the PIRS were calculated as described in Fig. 4*B* and 5*A*, respectively. In 17 of the 77 SCs recorded, kynurenic acid (2 mM) and picrotoxin (100 µM) were dissolved into extracellular recording solution to block glutamatergic and GABAergic synaptic transmission, respectively. No significant (qualitative or quantitative) differences were observed in these recordings. I_h was blocked in (n = 2) cells with 10 µM application of ZD7288 (Tocris, Sigma) in the extracellular bath solution.

Signals were sampled at 20 kHz using Clampex 10.0 (Axon Instruments) and recorded with a Multi Clamp 700B amplifier by Axon Instruments. Higher sampling rates were used for illustration purpose. Stimulating current protocols were designed using subsequent pCLAMP current square pulses of different amplitudes (0-1000 pA, with increments of either 25 or 33 pA) and durations (10-50ms, with 10 ms increments), the cellular holding voltage (-40 to -80 mV) was modulated within a physiological ranges. Hyperpolarizing synaptic currents were simulated with a double exponential function:

$$I_{Syn} = e^{(-t/\tau 1)} - e^{(-t/\tau 2)}$$

where τ1 and τ2 are the rise and decay time constants were set at 1 ms and 5 ms, respectively. Simulated synaptic inputs of increasing magnitude (from -25 pA to -500 pA, Δ = -25 pA) were separated by a 500 ms baseline current (DC). In another experimental condition we investigated the effect of GABAergic temporal summation leading to PIRS (Fig. 7*C-D*) by simulating multiple desynchronized (noise = 1)

inhibitory synapses (1 to10 synapses, 100 pA each) within the duration of half of a theta cycle (*i.e.,* 60 ms).

A MATLAB generated chirp stimulation (with frequency changing linearly from 0 to 20 Hz in 20 seconds, steady amplitude ranging between 10 and 100 pA in different neurons) (Erchova et al., 2004) was used to investigate the intrinsic resonance frequency of the cell. In some papers, this is known as a ZAP stimulus. Sag ratios were calculated by dividing the peak trough membrane voltage by the steady state membrane voltage (Giocomo and Hasselmo, 2009).

SCs were identified based on their somatic/dendritic anatomical location (LII), *post-hoc* morphology recovery, and electrophysiological signatures (Alonso and Llinás, 1989; Alonso and Klink, 1993; Dickson et al., 2000; Heys et al., 2010) such as, resting membrane potentials (< -55 mV), input resistances (< 120 MΩ), strong sag potentials (average ratio = 1.069±0.037), subthreshold membrane potential oscillations, and cluster spiking. As selecting criteria for establishing recording quality we used series resistances (≤ 30 MΩ) and peak action potentials (> 0 mV)**.** Somas of PCs on the other hand, were typically located in LIII, were usually more hyperpolarized, with smaller sag ratios (average ratio = 1.037±0.023), and unable to display subthreshold membrane potential oscillations.

Histology

After the *in-vivo* and *in-vitro* experiments were performed, brain slices were postfixed in paraformaldehyde overnight. Biotin-loaded cells were visualized using avidin–biotin complex (Vectastain Elite ABC kit (Standard), #PK-6100; Vector Laboratories) and DAB reactions (DAB Peroxidase Substrate Kit, #SK-4100; Vector Laboratories). The sections were mounted on gelatin-coated slides. The *in-vivo* slices were also counterstained with Neutral Red or Cresyl Violet.

Data analysis

All *in-vivo*, *in-vitro*, and *in-silico* analyses have been performed using a combination of scripts implemented in MATLAB (Natick, MA Version 7.9, 2009), R, or Microsoft Excel. A MATLAB script was used to extract the 10 ms of voltage data preceding each spontaneous AP. A sliding window in Excel calculated the average derivative of the voltage over 0.5 ms. The IPSP maximum and minimum were found by extracting the voltage values where the derivative of the voltage crossed 0 downward or upward, respectively (see Fig. 2*C*). Putative IPSPs were extracted and analyzed in terms of amplitude (*i.e.,* maximum-minimum voltage values) and delay of the spike (from the IPSP onset, *i.e.,* maximum voltage value) using R. An IPSP was defined as the largest hyperpolarizing voltage deflection larger than -0.2 mV within the 10 ms preceding the spike. Regular APs were separated by PIRS based of the presence of at least one putative IPSP in front of the spike. Examples of IPSPs of different amplitudes can be found in Fig. 2*D* together with a density plot distribution of all the IPSPs amplitudes recorded *in-vivo*.

Computational Model

The biophysical model presented here builds on previous models (Hasselmo 2013; Fransén et al., 2004; Ferrante, 2012) and expands them by using a full set of 22 fully reconstructed mEC-LII-SC morphologies (Garden et al., 2008) and 13 types of active properties (Fransén et al., 2004). Model, neuronal morphologies, ion channels and simulation files are publically shared in the ModelDB section of the SenseLab database (accession number: 155708).

Model and simulations were implemented and run in NEURON Simulation Environment (Hines and Carnevale, 1997) v7.3 with variable time step on a 32-bit Xeon (2.53 GHz) quad-core Dell Precision T3500 under Windows 7. Active properties included in the model: a variant of the Hodgkin-Huxley formalism consisting of a fast sodium channel (I_{Naf}) and an outward delayed rectifier potassium current (I_{Kdr}); four types of I_h kinetic conductances to represent a continuous variation along mEC DV cells (I_{hd} and I_{hv}) and the simultaneous presence of fast and slow (I_{hf} and I_{hs}) properties in each cell, as previously described in mEC SCs (in Table1 of Shay et al., 2012); a slowly inactivating persistent sodium channel

(I_{NaP}); three calcium-activated currents, an afterhyperpolarization potassium current (I_{Kahp}), a non-selective cation current (I_{CAN}), and potassium current (I_{KCa}); a long-lasting voltage-sensitive calcium current (I_{CaL}); dynamic extracellular calcium accumulation (cacumm); and a passive leak (I_{leck}) for sodium, potassium, calcium, chloride, and magnesium currents. After fine tuning the model with the above mentioned currents we turned off all the currents that were unnecessary to replicate the experimental evidences. Therefore, for all simulations shown in this article we used a basic set of six ion channels: I_{Naf}, I_{Kdr}, I_{hd}, I_{hv}, I_{hf}, and I_{hs}. Unless otherwise noted, active and passive properties were uniformly distributed along the neuronal surface and their maximum conductances were tuned to fit the experimental results. Ionic channel kinetic parameters have been previously published (Shay et al., 2012) (and can also be retrieved from senselab.yale.med.edu/ModelDB).

RESULTS

Strong sag responses and high resonant frequencies suggest prominent I_h conductances in SCs

To probe the ability of mEC-LII-SCs (Fig. 1*A*) to generate PIRS *in-vivo* in anesthetized rats we recorded for 100 seconds the intracellular voltage of 15 cells from 15 different animals at peri-AP-threshold so that synaptic potentials could generate spontaneous APs (Fig. 1*B*). We then stimulated each cell on average 4 times (number of trials = 59) with a 1000 pA hyperpolarizing current step lasting 2 seconds (as Fig. 1*B* inset). The hyperpolarizing stimulation produced pronounced sag responses in all SCs, and PIRS in about half of the trials (29 out of 59 trials, 49.1%). This result suggests that strong hyperpolarizing inhibitory input could generate PIRS in mEC-LII-SCs *in-vivo*.

I_h induces rebound spiking following inhibitory inputs (PIRS)

I_h is one of the possible intrinsic mechanisms responsible for sag and rebound potentials. During in vitro experiments, we tested if blocking I_h (with ZD7288) in high (7.8 Hz) and in low (1.94 Hz) resonant frequency SCs would be sufficient to stop the cells ability to produce PIRS for the all range of inhibitory inputs. Blocking I_h prevented the two SCs from showing resonance (Fig. 1*C*).

Blocking I_h also made SCs unable to generate PIRS in response to hyperpolarizing current steps of different amplitudes (Fig. 1*D*). As expected, in both cells ZD7288 significantly reduced the amplitude of the sag responses as a function of the inhibitory stimulus amplitude (Fig. 1*E*) and slowed down their sag time constant (Fig. 1*E*, insets). For both cells (with or without ZD7288) the amplitude of the stimulus was highly predictive (linear correlations, $R^2 > 0.86$) of the amplitude of the sag. These results suggest that in mEC-LII-SCs, I_h is a necessary mechanism for PIRS generation.

Spontaneous *in-vivo* APs are often preceded by IPSPs, suggesting they may be PIRS

We then analyzed the 10 ms preceding the generation of each spontaneous AP during *in-vivo* recording (378 spikes coming from 5 distinct cells, total recording = 600 s) to look for evidence of IPSPs immediately preceding the APs (Fig. 2*A,B*). An IPSP was defined as the largest hyperpolarizing voltage deflection (larger than -0.2 mV) within the 10 ms preceding the spike. To automatically identify the IPSPs we used a 0.5 ms sliding window to calculate the average derivative of the voltage in the 10 ms preceding the spike. The amplitude of each IPSP was calculated by subtracting the IPSP minimum (the voltage value where the derivative of the voltage crossed 0 upward) from its maximum (the voltage value where the derivative of the voltage crossed 0 downward) as in Fig. 2*C*. The delay of the spike was calculated from the IPSP onset (*i.e.,* maximum voltage value). We expected a monotonically upward change in the graded potential preceding the AP threshold, but surprisingly, we found that most of the APs (62.4%) were immediately preceded by at least one putative IPSP (Fig. 2*B-D*). To ensure that the hyperpolarizing inflections in the membrane potential were GABAergic in nature (rather than due to the absence of excitation) intracellular picrotoxin was used to block $GABA_A$ receptors. Intracellular picrotoxin reduced the number of IPSPs preceding the AP to 13.5% (Fig. 2*E*). Notably, intracellular picrotoxin did not significantly affect the average amplitude of the IPSP, but only the likelihood that a spike was a putative PIRS (Fig. 2*E*). Perhaps because picrotoxin was administered intracellularly, it is possible that due to limits of diffusion, a small subset of $GABA_A$ receptors (the ones that were more distal from the

soma/pipette) were not blocked by Picrotoxin, hence their amplitude remained the same. These results (Fig. 2*E*) hint that *in-vivo* most of the APs in mEC-LII-SC are immediately preceded by one or more IPSPs. Furthermore, this phenomenon can be down-regulated by intracellular picrotoxin suggesting that the biophysical mechanism responsible for the *in-vivo* emergence of PIRS may be the $GABA_A$ (rather than $GABA_B$) receptor.

We also tested if IPSPs were facilitating the AP generation by asking if the amplitude of the IPSP predicted the timing of the spike (Fig. 2*F*). In the control condition, IPSPs larger than the median (0.5 mV) were followed by significantly shorter PIRS delays (4.0±2.63 ms, n=118) compared to IPSP smaller than the median that produced on average longer PIRS delays (4.8±2.75 ms, n=118). This result suggests that larger IPSPs play a functional facilitating role in the generation of the APs. With picrotoxin the significance of this relationship was lost and the few PIRS recorded were significantly slower compared to the control condition, both for small and large IPSPs (Fig. 2*F*). Because we adjusted the base current to keep the neuron at peri-AP-threshold, the firing output between different experiments (*e.g.,* between control and picrotoxin conditions) is not comparable.

When mEC-LII-SCs approach the threshold to generate an AP, timely arrival of IPSPs could have an excitatory effect due to the depolarizing phase of their rebound potentials. Furthermore, GABA may differentially affect the cellular threshold to generate an AP, as well as, the cellular firing output in response to the same excitatory input. In order to test these hypotheses and circumvent the limitations of our previous approach we slowly (linearly) increased and then decreased the excitatory current injected in the cells (in a ramp stimulation) and recorded the threshold necessary to generate an AP *in-vivo,* in control and in intracellular picrotoxin conditions. Surprisingly, blocking $GABA_A$ receptors resulted in higher current thresholds necessary to initiate an AP (Supplementary Fig. 1*A,B*) while simultaneously making these cells more excitable across all input strengths, both at the single cell (Supplementary Fig. 1*C* left panel) and at the population (Supplementary Fig. 1*C* right panel) level. This last line of evidence suggests that GABA inputs can make mEC-LII-SCs more likely to fire an AP while concurrently constraining their maximum firing rate as well as their total number of spikes.

Neuronal voltage state, as well as, inhibitory stimulus duration and amplitude, affect the delay and the number of PIRS

The delay of the spike in response to an inhibitory input can be differentially affected by the present neuronal membrane voltage, as well as by the amplitude and duration of the inhibitory inputs. This kind of analysis requires the exploration of a large dataset of neuronal input/output relationships that are simply unattainable *in-vivo,* hence we recorded intracellularly from *in-vitro* slices of mEC-LII-SCs (Fig. 3*A*). Specifically, we systematically and independently altered the amplitude and duration of a hyperpolarizing (current step) stimulus, as well as the holding voltage of the cell to study how these changes affected the timing of the PIRS (Fig. 3*B*). It is important to notice that these current step stimuli are intended to mimic barrages of inhibitory stimuli of different durations and amplitude, not single inhibitory synapses. Independently of the stimulus duration and the holding voltage, larger amplitude hyperpolarizing inputs systematically produced PIRS with shorter and less variable delays (Fig. 3*C,D*), with a consistent shape of the function following a power law as presented in the figure legend. This was one of the most important properties to test for modeling.

Across all the stimulus amplitudes, shorter duration inhibitory stimuli resulted in longer PIRS delays (Fig. 3*C*). For instance, halving the duration (from 40 ms to 20 ms) of a 500 pA stimulus made its PIRS delay ~270% longer (from ~37 to ~100 ms). This effect was more substantial for weaker stimuli and diminished as inputs grew stronger. Similarly, for the same input amplitude (500 pA), a mere 5 mV difference in the baseline membrane voltage (-59 and -64 mV) produced a 20 ms difference (*i.e.,* 44% slower) in the delay of the PIRS (from 45 to 65 ms, respectively) as shown in Fig. 3*D*, top panel. Hence, compared to hyperpolarized states, more depolarized voltages (*e.g.,* -59 mV) produced shorter PIRS delays but this was true only with larger stimulus amplitudes (*e.g.,* 500 pA). Indeed, more depolarized states were usually the only ones enabling PIRS with weaker stimuli (*e.g.,* 200 pA) and those produced much longer PIRS delays (120 ms). This is an important consideration for interpreting the cell population

results that will be presented later on (in Fig. 4*C*) where depolarized states on average produced slower and more variable PIRS. Furthermore, intrinsic cellular differences (Fig. 3*C,D*, top vs. bottom panels) made the delay in PIRS response to a similar input duration (*e.g.,* 20 ms) or holding voltages highly variable across cells for all stimulus amplitudes. The relationship between the amplitude of the stimulus and PIRS delays (at each specific stimulus duration and voltage state), can be described by power laws ($0.6 < R^2 < 0.99$). This data suggest that across all stimulus amplitudes, PIRS have shorter delays and are temporally more precise when the cell is depolarized and when the afferent hyperpolarizing inputs are stronger or longer lasting.

Given the same inhibitory input mEC-LII-SCs may vary widely in the number of PIRS generated (Supplementary Fig. 2). These differences may play a role in the cellular firing frequency output, as well as in the functional rage of inhibitory input to which the cell responds. We asked what range of stimulus amplitudes allows the transition from 0 to 1 (or more) PIRS at different stimulus durations. Long lasting stimuli (*e.g.,* 50 ms) can recruit a cell with weaker stimulus amplitudes (Supplementary Fig. 2*B* top left panel). Moreover, compared to brief inputs (*e.g.,* 30 ms), long inputs (*e.g.,* 50 ms) allow for more rapid transitions from 0 to multiple PIRS (265 vs. 436 pA for 20 and 50 ms, respectively). Some mEC-LII-SCs are able to functionally span a wide range of input amplitudes (~600 pA) while others can only operate in a very narrow range (~230 pA) saturating their output (number of elicited spikes) fairly quickly (compare Supplementary Fig. 2*B* top left vs. bottom left panel). For specific input amplitudes, long lasting stimuli tend to produce more PIRS. Conversely, compared to baseline currents that shift the membrane potential to peri-AP-threshold voltages, hyperpolarized membrane potentials recruited cells with weaker inputs and simultaneously extended the functional range of input amplitudes to which the cell responds (Supplementary Fig. 2*B* right). Furthermore, in agreement with the fact that more hyperpolarized states have more I_h activated, they tend to fire more PIRS given the same inhibitory stimulus.

Efficiency of inhibitory stimuli as a mechanism for spike generation in mEC SCs

How efficient is the inhibitory-driven mechanism compared to the traditional depolarization-induced mechanism in generating APs? To answer this question we compared the outputs (F-I curves) of depolarizing (Supplementary Fig. 3*A*) and hyperpolarizing (Fig. 3 and Supplementary Fig. 2) current steps. Similar to PIRS, depolarization-driven AP delays were also highly affected by intrinsic cellular differences (Supplementary Fig. 3*B*, left and right panels). For instance, given the same holding voltage (-59 mV) and stimulus amplitude (230 pA), Cell#73 was about 5 times faster than Cell#17 in generating an AP (5 vs. 26 ms, respectively). At the single cell level, most depolarization induced APs were fast (<20 ms) if compared to PIRS (see Fig. 3 for comparison). This is due to the fact that even when starting from the same holding voltage, depolarizing stimuli bring the potential much closer to threshold. This single cell result was confirmed at the population level (Supplementary Fig. 3*D* left). On average the cells transitioned from 0 to multiple spikes in a narrower range of stimulus amplitudes for the excitatory stimuli (Supplementary Fig. 3*C*) compared to the inhibitory ones (Supplementary Fig. 2*B*). Surprisingly, small (<200 pA) inhibitory stimuli were more effective than excitatory stimuli in eliciting a spike (Supplementary Fig. 3*D*, right), but the opposite was true for larger stimuli (>200pA). These results suggest that although with a slower time course, inhibition in mEC-LII-SCs can be more effective than excitation in eliciting APs.

Intrinsic differences between SCs and PCs affect PIRS firing properties

Intrinsic differences between and within cell classes may affect the PIRS properties. To quantify these differences we recorded how changes in stimulus amplitude, stimulus duration, and overall cellular voltage state affect the population of mEC-LII-SCs (n = 77; Fig. 4*A* left) and mEC-LII/III-PCs (n = 7; Fig. 4*A* right). To perform this analysis, an extensive dataset of current step experiments was collected, n = 9276 for mEC-LII-SCs and n = 2727 for mEC-LII/III-PCs. The stimulus amplitude produced only minor differences between SCs and PCs in the PIRS delay (Fig. 4*B*, top), but greatly affected the differences in the number of PIRS (Fig. 4*B*, bottom). Indeed, 1 nA change in stimulus amplitude (25-1000 pA) produced small differences in the average number of PIRS (from 0.14 to 0.52) of PCs when

compared to SCs (from 0 to ~2 PIRS). These results suggest that compared to PCs, SCs are much more responsive to strong inhibitory inputs; but when PCs fire in response to inhibition their timing is similar to SCs. Similarly, the PIRS firing output of the SCs is more voltage-dependent and prefers more depolarized voltages (around -54.5 mV) while PCs reach their peak PIRS firing rate at about -57.7 mV (Fig. 4*C* bottom). For instance, at -70 mV about 1/4 of both PC and SC trials generated PIRS, but while PCs did not dramatically change that number across the range of membrane voltages, SCs quadrupled their rate of PIRS output at -50 mV. This data suggests that at the population level as SCs become more depolarized, they fire a greater number of PIRS compared to PCs. Additionally, the delay of PIRS in SCs (and PCs) increases as the membrane potential depolarizes; for instance, at -65 mV the average PIRS delay of SCs is ~35 ms, while at -40 mV it slows down to ~80 ms. Lengthening the duration of the stimulus led to a monotonic decrease in the PIRS delay for SCs and PCs (Fig. 4*D* top). Despite this similarity, compared to PCs, SCs tended to fire more PIRS when the stimulus duration was between 30 and 60 ms (Fig. 4*D*, bottom) and significantly less when that duration was both increased and reduced. This time course was consistent with the average SC sag time constant (see Fig. 1*E* inset) that provided the extra driving force to elicit PIRS.

Dorso-ventral differences in SCs and PCs relevant to grid cell firing

SCs have different resonant and intrinsic properties that vary along the mEC DV-axis (Giocomo et al., 2007; Giocomo and Hasselmo, 2009). For this reason we decided to investigate how SCs and PCs resonance frequency at rest (around -60 mV) and their mEC DV position affected the rebound spiking properties. Compared to PCs, SCs tend to resonate at higher frequencies (Fig. 5*A*). Unlike PCs, the average number of PIRS for SCs was affected by the DV position (Fig. 5*B*). Dorsal cells (2.6 mm) fired on average 0.38 spikes on each trial (38%) while ventral (6.7 mm) fired on average 0.71 spikes for each trial (71%). PIRS of SCs came at slower and more variable delays in more ventral positions while PCs showed faster delays along the same axis and kept their noise level constant. On average, PIRS of neurons (for both PCs and SCs) resonating at high frequencies were quicker and more temporally constrained (Fig. 5). Consistent with previous results (Schreiber et al., 2004) PCs on average exhibited lower resonance strengths (*i.e.,* q-values (Hutcheon et al., 1996)) compared to SCs, therefore, even PCs with high resonant frequencies (>3 HZ) had an overall weak resonant response. Overall these results suggest that PIRS properties in SCs are modulated along the DV axis ad that such gradients are consistent with the gradient in grid cell scaling seen along the same axis (Hafting et al., 2005; Brun et al., 2008).

Given the same inhibitory input SCs produced a larger and quicker sag response (compared to PCs) (Supplementary Fig. 4*A*), which differentially affected the cell's probability to generate a PIRS. In particular, for weak inputs the sag amplitude of SCs and PCs was similar but as the input grew larger SCs produced a more pronounced sag response (Supplementary Fig. 4*B* left). Similarly, PCs sag time constant was a lot slower compared to SCs and the time constant of SCs became faster for stronger inputs suggesting a voltage-dependent effect that was not present in PCs (Supplementary Fig. 4*B* right). Indeed, even at the population level the amplitude of the SC sags and their time constant were highly correlated with the average number of PIRS (Supplementary Fig. 4*C,D*). The same was not true for PCs. Consistently, SCs with large and fast sag responses produced faster PIRS; while this relationship was less clear in PCs. The striking difference in PCs and SCs sag and resonant responses suggest that I_h is expressed more in SCs.

PIRS dendritic propagation and mEC DV differences relevant to grid cells

The site of initiation and the direction of propagation of an AP are crucial to understand the integrative actions of mammalian neurons in the CNS. This is because multiple AP initiation sites within a neuron may explain how neuronal firing may be controlled by both excitatory and inhibitory inputs as well as by their active properties. To shed some light on this issue we implemented 22 biophysically realistic computational models (Supplementary Fig. 5*A,F*) of mEC-LII-SCs. The model was validated against different sets of experimental data, such as, I_h resonance properties at the cellular level

(Supplementary Fig. 5*B,C*), PIRS timing response to different stimulus amplitudes (Supplementary Fig. 5*D,E*), and mEC DV differences in resonance frequency (Supplementary Fig. 5*F,G*).

Some feed-forward inhibitory interneurons (*e.g.,* PV+ cells) make synaptic contacts in the perisomatic region of principal cells while others may target the dendritic region (*e.g.,* SOM+ interneurons). This may lead to distinct functional consequences in buffering the neuronal input/output of principal cells (Ferrante and Ascoli, 2015). Previous studies (Stuart et al., 1997) have shown that in the central nervous system, inhibition is concentrated precisely at the location where it is best suited to inhibit action potential initiation (*i.e.,* close to the hillock segment). On the other hand, the expression of large I_h conductances in mEC stellate cells could enable the generation of PIRS. This could have important consequences for the synchronization of action potential between excitatory inputs arriving in the dendrites and inhibitory inputs arriving in the somatic region. For this to happen, PIRS need to be able to travel from the soma back to the dendrites. Our simulations (Fig. 6*A*) suggest that mEC cells show little attenuation in the backpropagation of PIRS (Fig. 6*B,C*). Note that it is difficult to distinguish somatic (black) and dendritic (gray) voltage traces as they are mostly overlapping. Unlike other currents, such as I_{KA} (Migliore et al., 2005), but consistent with previous experimental data on AP backpropagation in hippocampal CA1 PCs (Magee, 1998), increasing I_h distribution with the distance from the soma only moderately affected back propagation of PIRS (Fig. 6*C*).

We then asked if the intrinsic differences in SC neuronal morphologies (Garden et al., 2008) or I_h kinetic properties (Shay et al., 2012) recorded experimentally along the DV axis of the mEC were responsible for the DV gradient observed in PIRS delay (Fig. 5*B* top left panel). Neuronal morphology and I_h properties played a compensatory effect in regulating the PIRS delay, with the I_h effect more closely resembling the experimental trend (Supplementary Fig. 6) while the morphology opposed the trend. Forward propagation of PIRS (Supplementary Fig. 7*A,B*) on the other hand, allowed the stimulated branch to fire twice, first in response to the inhibitory stimulus (PIRS) and later, when the backpropagating PIRS reinvaded the branch after reaching the soma. This mechanism could be used for selectively strengthening synapses of branches that fire PIRS. When the dendritic distribution of I_h was uniform, a narrow range of stimulus amplitudes (50 pA, from 425 to 475pA) enabled most branches (from 25% to 93%) to fire PIRS (Supplementary Fig. 7*C*). On the contrary, increasing the distribution of I_h with distance from the soma made the dendrites less prone to generate PIRS and even strong hyperpolarizing stimulation (1000pA) elicited PIRS in only 39% of the branches. This prediction seems to suggest that the distance-dependent rule of I_h distribution observed in other hippocampal dendrites (Magee, 1998) would impair the ability of distal dendrites to generate PIRS but it is also possible that compensatory (distance-dependent) changes in the distribution/expression of AMPA, NMDA (Menon et al., 2013) or GABA receptors could normalize this difference between proximal and distal branches. Indeed, despite this difference in the current necessary to elicit a PIRS, the voltage thresholds in all dendrites were remarkably similar for the two dendritic distributions of I_h (Supplementary Fig. 7*D*). This result suggests that expression/regulation of I_h could be a potential mechanism to enhance or counteract the dendritic ability to fire PIRS. Our model finally suggests that unlike in the somatic recordings, dendrites would require strong activation of $GABA_B$ receptors which have lower equilibrium potential (-95 mV) to elicit spikes in most (70%) branches, assuming uniform I_h distribution (Supplementary Fig. 7*D*) while $GABA_A$ receptors would only produce PIRS in a small percentage (10%) of branches.

It is important emphasize that despite the different spatial distribution of I_h (uniform or linearly increasing with distance from the soma) the two models that we present here (in Fig. 6 and Supplementary Fig. 7) have the same total amount of I_h conductances expressed in the cell. Our model suggests that, while a moderate amount of I_h is necessary to generate PIRSs, too much I_h may prevent them from happening. This is consistent with the fact that increasing the I_h conductance lowers the cellular input resistance (van Welie et al., 2004). Indeed, lowering the input resistance means that larger hyperpolarizing inputs are necessary to displace the same amount of voltage and generate a PIRS. This is particularly an issue in distal dendrites particularly if we assume that the spatial I_h distribution linearly increases with distance from the soma.

Can the amplitudes of the synaptic conductances and their temporal interactions predict the generation of PIRS?

In experiments, we were interested in testing the effect of more realistic synaptic stimuli (*i.e.,* double exponential kinetic currents for the rise and decay phases) on stellate cells PIRS generation *in-vitro*. To test this in experiments, we somatically delivered synaptic inputs (Fig. 7*A*) of increasing amplitudes (from -25 pA to -500 pA, Δ = -25 pA) separated by a 500 ms baseline current. For each cell we recorded 20 trials, each 12-second long at peri-AP-threshold. These experiments (see Fig. 7*A-B*) show that the probability of PIRS following single synaptic potentials goes up when the amplitude of the IPSP increases from -25 to -100 pA, values consistent with previous experiments (Deng and Lei, 2007). The recruitment of synchronized GABAergic cells is common in neocortex (Benardo, 2007). We also tested the effect of synchronized incoming GABAergic synapses using larger hyperpolarizing synaptic currents (100-500 pA). Going from a -25 to a -500 pA in synaptic amplitude more than tripled the probability to generate a PIRS (from 65% to 330%) with a clean linear correlation (R^2 = 0.79).

We also wanted to test how temporal summation of inhibitory synaptic inputs affects the generation of PIRS? To answer this question we increased the number of synaptic inputs (1-10 synapses, 100 pA each in amplitude) delivered within an interval of 60 ms and recorded the probability of generating a PIRS (Fig. 7*C-D*). In this context, 100% spike probability refers to the spontaneous firing rate without hyperpolarizing current stimulation. Going from 1 to 10 synaptic inputs doubled the probability of generating a PIRS (from 250% to 500%) with a clean linear correlation (R^2 = 0.69). Data reported in Fig. 7*B* and 7*D* are recorded at peri-AP-threshold but because their holding voltages were different, it is difficult to compare these two datasets. In short, these data suggest that realistic synaptic inputs might have a strong effect in generating PIRS in SC near threshold. Particularly, this last piece of evidence suggests that strong and temporally clustered synaptic inputs may play a synergistic role in enabling SC to fire PIRS.

DISCUSSION

Post-inhibitory rebound is a period of increased neuronal excitability following the cessation of inhibition. When the hyperpolarization generated by the activation of inhibitory synapses is removed the slow offset of the I_h current increases the level of a slow depolarizing current, giving rise to the characteristic sag and overshoot, and providing a mechanism for generating post-inhibitory rebound spikes (PIRS). We performed *in-vivo* and *in-vitro* intracellular recordings (supported by a biophysically realistic computational model) modulating the neuronal holding voltage, the amplitude and duration of hyperpolarizing stimulation in cells from slices at different positions along the mEC DV axis. Furthermore, this study links inhibitory hyperpolarizing input features (*i.e.,* amplitude and duration) and cellular properties (*i.e.*, neuronal morphology and ion channels) to investigate the emergence of spiking outputs (PIRS) possibly relevant for spiking responses of grid cells.

Recent experimental data suggest that principal (stellate) cells in the mEC-LII grid cell network, mostly receive recurrent inhibitory inputs that, coupled with uniform excitation, would be sufficient to generate stable grid cell firing (Couey et al., 2013). Our findings build on these observations by proposing that mEC-LII-SCs may fire in response to inhibition, using their active property, I_h, to produce depolarizing rebounds and spikes. Septal neurons project into entorhinal cortex (Alonso and Köhler, 1984) including projections from medial septal GABAergic cells (Köhler et al., 1984; Mizumori et al., 1992). Additionally, during spatial navigation the firing frequency of cells in the medial septum is modulated by speed (King et al., 1998) and head direction (Welday et al., 2011). These GABAergic inputs from medial septum could regulate the timing of mEC interneurons to cause PIRS at specific time points on the theta cycle (Shay et al., 2015). The ability of the medial septum to relay speed and directional information into the mEC can be a potential mechanism for grid cell formation (Hasselmo, 2013). For this reason we tested the modulation of the inhibitory inputs into the mEC neurons.

In particular, we believe the *in-vivo* data (Fig. 2) to be particularly relevant because it suggests that the generation of APs *in-vivo*, in mEC-LII-SCs might be regulated by the activity of inhibitory interneurons. Although this seems reasonable there are at least two alternative explanations to why SC

firing tends to be preceded by IPSPs: (1) that fast spiking interneurons and SCs share the same source of excitatory inputs generating spikes in both cell types, FS cells fire before stellate cells and project to them; and (2) that reciprocal connections between SCs and interneurons generate fast oscillations where SCs spiking always follows inhibitory input, but is in fact caused by external excitatory inputs to SCs. Our data does not differentiate between these alternative and non-mutually exclusive hypotheses but we believe that probability of generating PIRS may be enhanced in feed-forward inhibitory networks where I_h is expressed. Also, Fig. 2B-D shows an ongoing cellular depolarization prior to spiking regardless of IPSP input, in both control and picrotoxin conditions. Thus, while PIRS may contribute to the generation of APs in mEC SCs, these data do not suggest that they are either necessary or sufficient.

Furthermore, the fact that we observed (in Fig. 4*D*) a narrow stimulus duration that enhances cellular response (or PIRS generation) is consistent with *in-vivo* recordings showing that mEC-LII-SCs preferably fire in a narrow phase of theta (Quilichini et al., 2010; Domnisoru et al., 2013; Schmidt-Hieber and Häusser, 2013) and *in-vitro* results showing that the preferred phase-locking of spikes to theta inputs is enhanced by excitatory and inhibitory synaptic inputs (Fernandez et al., 2013). The results are also consistent with recent *in-vitro* and *in-vivo* data from our lab showing that SCs have a specific phase range of the theta cycle (*i.e.,* between the peak and subsequent descending zero crossing) where incoming hyperpolarizing synaptic inputs elicit PIRSs (Shay et al., 2015; Tsuno et al., 2015). Interestingly, a recent study (Tang et al., 2014) suggests that weakly theta-locked spiking border cells are mostly mEC-LII-SCs, and strongly theta-locked spiking grid cells are mostly mEC-LII-PCs.

Surprisingly, unlike our previous observations in simulations (Migliore et al., 2004; Migliore et al., 2005; Ferrante et al., 2013) showing that excitatory inputs easily generate dendritic spikes on tiny dendrites (due to high input impedance) when coupled with I_h, here we report that PIRS are more easily generated on larger volumes (*i.e.,* perisomatic regions), due to the strong dendritic compartmentalization of I_h.

Together, our data suggest that the synergistic interaction between strong (and/or highly timed) incoming hyperpolarizing inhibitory inputs and intrinsic properties of I_h could allow for the emergence and modulation of grid cell firing. In general, our *in-vivo* and *in-vitro* results do not challenge the mainstream hypothesis that grid cells require the excitatory driving force from the hippocampus (Bonnevie et al., 2013). They, on the other hand suggest that excitatory inputs may work in tandem with inhibitory inputs activating I_h to promote grid cell firing during spatial navigation.

ACKNOWLEDGMENTS

We thank Drs. Giorgio A. Ascoli, Michele Migliore, Nancy Kopell, Howard Eichenbaum, James R. Hinman, and all the members of Dr. Hasselmo's laboratory for helpful discussions and comments on this work. We thank Dr. Jim Heys for technical assistance and initial training. This work was supported by NIH Grant MH60013, NIH grant MH61492 awarded to M.E.H. The authors declare no competing financial interests.

Correspondence should be addressed to: Michele Ferrante, 2 Cummington Mall, Boston 02215, MA. Ph. 339-223-2340, mferr133@bu.edu

Figure Captions

Figure 1. *In-Vivo* and *In-Vitro,* Evidence and Pharmacological Modulation of Putative Post-Inhibitory Rebound Spikes (PIRS). ***A***, *Left*, parasagittal histological slice after *in-vivo* recording, mEC-LII cell bodies are visible, hippocampus (HC), lateral entorhinal cortex (LEC), perirhinal cortex (PRh), and visual areas (VI/II) are also labeled for reference. *Right,* higher magnification showing a morphological identification of a biocytin-labeled mEC-LII-SCs and mEC Layer I-III (LI/III). ***B***, *Left*, Voltage traces showing spontaneous spikes, and a post-inhibitory rebound spike (current step amplitude = -1000 pA). *Right*, Post-inhibitory rebound spike (PIRS) magnification showing sag and rebound potentials. Spike truncated. ***C***, Neuronal resonance before (left) and after (right) bath administration of I_h blocker

(ZD7288). Bottom right inset shows change in peak resonant frequency after blocking I_h. ***D***, Number of PIRS before (black) and after blocking I_h (gray) for two distinct neurons (empty vs. filled circles). Lines are second order polynomial fits to Cell#50 (solid line) and Cell#51 (dashed line) with R^2 values reported on top. ***E***, Sag ratio before (black) and after blocking I_h (gray) for two distinct cells (empty vs. filled circles). Lines are linear fits, with the lower limit of R^2 reported for the two cells in control condition (black lines above) and during ZD7288 administration (gray lines below). *Top left inset*, example of between-cells time constant variability as a function of stimulus amplitude. *Bottom right inset*, mEC LII SC time constant when ZD7288 was applied.

Figure 2. *In-Vivo* Pharmacological Modulation of Inhibitory Post-synaptic Potentials and PIRS Delay. ***A***, Perithreshold voltage traces showing spontaneous APs in control condition (*left*), and during the effect of intracellular $GABA_A$ non-competitive channel blocker picrotoxin (*right*). ***B***, Higher magnification of the spikes from the marked rectangle for each condition. The AP in the intracellular picrotoxin conditions (in gray) is characterized by a monotonic increase (building up phase) of the voltage over time. In control conditions (black), neurons tend to show a post-inhibitory rebound spike, as indicated by spiking associated with a pronounced inflection of the voltage within the 10 ms preceding the spike. ***C***, a sliding window computed a smoothed (over 0.5 ms) derivative of the voltage before the spike to identify the points of maximum (/onset) and minimum (/termination) of the putative IPSP. ***D***, Density plot of the IPSP amplitudes for the control case (median = 0.5 mV). Inset shows three sample IPSPs of different amplitudes (blue = 0.4 mV; red = 0.87 mV; gray = 1.3 mV) recorded from the same neuron. ***E***, Left, probability to find an IPSP in the 10 ms preceding the spike. Fractions on top of the bar graph are PIRS/total number of spikes. Data are represented as mean ± SD, n = 6 neurons for the control condition and n = 6 neurons for the intracellular picrotoxin condition. Total time of the recording 600s for each condition). Right, IPSP amplitude in control condition (black) and with intracellular picrotoxin (gray). ***F***, PIRS delay for small (<0.5 mV IPSP amplitude) and large (>0.5 mV) IPSP amplitudes for control (black, n = 236) and intracellular picrotoxin (gray, n = 49) conditions. Black horizontal line depicts statistically significant difference ($p < 0.05$) error bars represent SEM.

Figure 3. *In-Vitro,* Single Cell Quantification of Stimulus-Dependent Changes in Post-Inhibitory Rebound Spike Delay. ***A***, Photomicrograph example of a mEC horizontal brain slice (2X magnification) with inset (on the bottom) showing a 20X magnification of a SC anatomy and morphology. ***B***, Hyperpolarizing current stimulation protocol. Holding current, stimulus duration, and amplitude were systematically changed to investigate their impact on the post-inhibitory rebound spike delay. ***C***, *Top*, Modulation of PIRS delay (y-axis) by stimulus amplitude (x-axis) and stimulus duration (different symbols) at -61 mV. Fitting lines are power functions. For 50 ms stimulus duration, PIRS delay = 5.57*(stimulus amplitude) $^{-0.834}$, while for 20 ms stimulus duration, PIRS delay = 28552*(stimulus amplitude)$^{-2.036}$. ***D***, *Top*, Modulation of PIRS delay (y-axis) by stimulus amplitude (x-axis) and holding membrane voltage (different symbols). At -59 mV, PIRS delay = 10.333*(stimulus amplitude)$^{-0.873}$, while at -64 mV, PIRS delay = 1929.7*(stimulus amplitude)$^{-1.656}$. **C-D**, *Bottom panels*, depict a different cell, to show examples of between-cell variability.

Figure 4. *In-Vitro,* mEC Neuronal Populations (LII-SCs Vs. LII/III-PCs), Differences in PIRS Properties. ***A***, Photomicrographs of mEC horizontal slices with insets (on the bottom) showing magnifications of a LII-SC (left) and a LII/III-PC (right) anatomy. ***B***, SCs (black, number of cells = 77) and PCs (gray, number of cells = 7) differences in PIRS delay (top) and average number of spikes (bottom) as a function of stimulus amplitude. Top, SCs (n = 2454, R = 0.395, $p < 0.01$), PCs (n = 558, R = 0.435, $p < 0.01$); bottom, each data point represents the average number PIRS for 120 square pulse stimulation experiments, SCs (n = 71, R = 0.909, $p < 0.01$), PCs (n = 21, R = 0.762, $p < 0.01$). Holding voltage = -60.3±7.3 mV; Stimulus duration= 42±31 ms. ***C***, Same as B, but as a function of membrane holding voltage. Top, SCs (n = 2454, R = 0.225, $p < 0.01$), PCs (n = 558, R = 0.497, $p < 0.01$); bottom SCs (n = 71, R = 0.758, $p < 0.01$), PCs (n = 21, R = -0.073, $p = 0.375$). Fitting lines (in **C-D**) are fifth order

polynomials, dotted lines describe preferred holding voltage to generate PIRS for the two cell populations. Stimulus amplitude = -321±190 pA; Stimulus duration= 42±31 ms. ***D***, Same as B but as a function of stimulus duration. Top, SCs (n = 2454, R = -0.388, $p < 0.01$), PCs (n = 558, R = -0.519, $p < 0.01$); bottom SCs (n = 47, R = 0.606, $p < 0.01$), PCs (n = 21, R = 0.895, $p < 0.01$). AP delays larger than 200 ms are not shown. Holding voltage = -60.3±7.3 mV; Stimulus amplitude = -321±190. To depict the full extent of the variability of the population response each panel shows the effect of one variable (*e.g.,* stimulus amplitude) when all the other variables (*e.g.,* holding voltage and stimulus duration) are independently manipulated.

Figure 5. *In-Vitro,* Influence of mEC Dorso-Ventral Position and Resonance Frequency on PIRS Properties of mEC-LII-SCs and mEC-LII/III-PCs. ***A*****,** Injected chirp (ZAP) stimulus (top left), resonance of a mEC-LII/III-PC (top right), resonance of a mEC-LII-SC (bottom right), impedance analysis for both cells and impedance curve fit to estimate the cell's resonant frequency from the peak of the curve (bottom left). ***B***, Impact of cellular position along the mEC DV axis on PIRS delay (Top) and average number of PIRS (Bottom) for SCs (black) and PCs (gray). Top panels, SCs (n = 2454, R = 0.085, $p < 0.01$) PCs (n = 558, R = -0.516, $p < 0.01$). Bottom panels, each data point represents the average number PIRS for 120 square pulse stimulation experiments for SCs (n = 9162, R = 0.067, $p < 0.01$) and PCs (n = 2689, R = 0.013, $p < 0.24$). ***C***, Influence of intrinsic cellular resonance frequency (at about -60 mV) on PIRS delay (Top) and average number of PIRS (Bottom) for SCs and LII/III-PCs. Top panels, SCs (n = 2454, R = -0.122, $p < 0.01$) PCs (n = 558, R = -0.693, $p < 0.01$); bottom panels SCs (n = 9162, R = 0.136, $p < 0.01$) PCs (n = 2689, R = 0.33, $p < 0.01$).

Figure 6. Simulations, Effects of I_h Dendritic Spatial Distribution on PIRS Backpropagation. ***A***, Schematic of the back propagation protocol in the computational model. PIRS back propagation was studied by eliciting a somatic PIRS with a brief hyperpolarizing current pulse. Stimulating electrode is placed somatically while voltage attenuation is recorded in each of the 84 dendritic compartments. Inset diagram shows the two dendritic distributions of I_h used, uniform and increasing with the distance from the soma (as experimentally observed in CA1 Pyramidal neurons in the hippocampus). ***B***, Voltage traces of a PIRS recorded locally in the soma (black) and distally in a dendritic branch (gray). Note that the two voltage traces are almost overlapping, showing little attenuation in the backpropagation of the PIRS from the soma to the distal dendrite. ***C***, The plot shows the peak AP amplitude along the dendrites of a mEC stellate cell model. Voltage attenuation with distance from the soma (back propagation) for uniform (left) and increasing distribution of I_h (right), as shown in the inset of panel A. This graph shows how the peak voltage of the spike differs during backpropagation from the soma into the distal branches.

Figure 7. *In-Vitro,* Synaptic Stimulus Amplitude and Temporal Summation Affect SC Ability to Generate PIRS. ***A***, Stellate cell displays rebound spiking in response to injected synaptic currents of different amplitudes (25-500 pA) near AP threshold. ***B***, Change in the probability of generating PIRS as function of the amplitude of the synaptic current injected (for 5 cells, 20 trials per cell) normalized against the control condition *i.e.,* no synaptic current injection (gray dotted line). Straight line represents linear fit. ***C***, Rebound spiking in response to temporal summation (within 60 ms) of multiple synaptic stimuli (1-10 stimuli, 100pA each). ***D***, Effect of the number of synaptic inputs integrating over time (60 ms) on the probability of generating PIRS (in 4 cells, 20 trials per cells) normalized against the control condition *i.e.,* no synaptic current injection (gray dotted line). Straight line represents linear fit.

References

Adhikari MH, Quilichini PP, Roy D, Jirsa V, Bernard C. 2012. Brain state dependent postinhibitory rebound in entorhinal cortex interneurons. J Neurosci. 32(19), 6501-10.

Alonso A, Klink R. 1993. Differential electroresponsiveness of stellate and pyramidal-like cells of medial entorhinal cortex layer II. J Neurophysiol. 70(1):128-43.

Alonso A, Köhler C. 1984. A study of the reciprocal connections between the septum and the entorhinal area using anterograde and retrograde axonal transport methods in the rat brain. J. Comp. Neurol. 225, 327-343.

Alonso A, Llinás RR. 1989. Subthreshold Na+-dependent theta-like rhythmicity in stellate cells of entorhinal cortex layer II. Nature. 342(6246), 175-7.

Ascoli GA, Gasparini S, Medinilla V, Migliore M. 2010. Local control of postinhibitory rebound spiking in CA1 pyramidal neuron dendrites. J Neurosci. 30(18):6434-42.

Beed P, Gundlfinger A, Schneiderbauer S, Song J, Böhm C, Burgalossi A, Brecht M, Vida I, Schmitz D. 2013. Inhibitory gradient along the dorsoventral axis in the medial entorhinal cortex. Neuron. 79(6), 1197-207.

Benardo LS. 1997. Recruitment of GABAergic inhibition and synchronization of inhibitory interneurons in rat neocortex. J Neurophysiol. 77(6):3134-44.

Bengtsson F, Ekerot CF, Jörntell H. 2011. In vivo analysis of inhibitory synaptic inputs and rebounds in deep cerebellar nuclear neurons. PLoS One. 6(4):e18822.

Bonnevie T, Dunn B, Fyhn M, Hafting T, Derdikman D, Kubie JL, Roudi Y, Moser EI, Moser MB. 2013. Grid cells require excitatory drive from the hippocampus. Nat Neurosci. 16(3):309-17.

Bottjer SW. 2005. Timing and prediction the code from basal ganglia to thalamus. Neuron. 46(1), 4-7.

Brun VH, Solstad T, Kjelstrup KB, Fyhn M, Witter MP, Moser EI, Moser MB. 2008. Progressive increase in grid scale from dorsal to ventral medial entorhinal cortex. Hippocampus. 18(12):1200-12.

Buetfering C, Allen K, Monyer H. 2014. Parvalbumin interneurons provide grid cell-driven recurrent inhibition in the medial entorhinal cortex. Nat Neurosci. 17(5):710-8.

Buzsáki G. 2002. Theta oscillations in the hippocampus. Neuron. 33(3), 325-40.

Buzsáki G, Draguhn A. 2004. Neuronal oscillations in cortical networks. Science. 304(5679), 1926-9.

Couey JJ, Witoelar A, Zhang SJ, Zheng K, Ye J, Dunn B, Czajkowski R, Moser MB, Moser EI, Roudi Y, Witter MP. 2013. Recurrent inhibitory circuitry as a mechanism for grid formation. Nat Neurosci. 16(3), 318-24.

Cunningham MO, Davies CH, Buhl EH, Kopell N, Whittington MA. 2003. Gamma oscillations induced by kainate receptor activation in the entorhinal cortex in vitro. J Neurosci. 23(30), 9761-9.

Deng PY, Lei S. 2007. Long-term depression in identified stellate neurons of juvenile rat entorhinal cortex. J Neurophysiol. 97(1):727-37.

Dickson CT, Magistretti J, Shalinsky MH, Fransén E, Hasselmo ME, Alonso A. 2000. Properties and role of I(h) in the pacing of subthreshold oscillations in entorhinal cortex layer II neurons. J Neurophysiol. 83(5), 2562-79.

Domnisoru C, Kinkhabwala AA, Tank DW. 2013. Membrane potential dynamics of grid cells. Nature. 495(7440):199-204.

Erchova I, Kreck G, Heinemann U, Herz AV. 2004. Dynamics of rat entorhinal cortex layer II and III cells: characteristics of membrane potential resonance at rest predict oscillation properties near threshold. J Physiol. 560(Pt 1):89-110.

Fernandez FR, Malerba P, Bressloff PC, White JA. 2013. Entorhinal stellate cells show preferred spike phase-locking to theta inputs that is enhanced by correlations in synaptic activity. J Neurosci. 33(14):6027-40.

Ferrante M. 2012. Dynamical Multiscale Models to Formulate Testable Predictions of Neuronal Computational Properties. Ph.D. Dissertation. George Mason Univ., Fairfax, VA, USA. Advisor Giorgio A. Ascoli. AAI3503977, ISBN: 978-1-267-27837-1.

Ferrante M, Ascoli G. 2015. Distinct and synergistic feedforward inhibition of pyramidal cells by basket and bistratified interneurons. Front. Cell. Neurosci. 9:439.

Ferrante M, Blackwell KT, Migliore M, Ascoli GA. 2008. Computational models of neuronal biophysics and the characterization of potential neuropharmacological targets. Curr Med Chem. 15(24), 2456-71.

Ferrante M, Migliore M, Ascoli GA. 2009. Feed-forward inhibition as a buffer of the neuronal input-output relation. Proc Natl Acad Sci USA. 106(42), 18004-9.

Ferrante M, Migliore M, Ascoli GA. 2013. Functional impact of dendritic branch-point morphology. J Neurosci. 33(5), 2156-65.

Ferrante M, Tahvildari B, Duque A, Hadzipasic M, Salkoff D, Zagha EW, Hasselmo ME, McCormick DA. 2015. Intrinsic Properties of Mouse Entorhinal Cortex Layer II/III Interneurons and Principal Cells Identify Seven Functional Groups. 2015 Neuroscience Meeting Planner, Program No. 672.14. Society for Neuroscience, Chicago, IL.

Fransén E, Alonso AA, Dickson CT, Magistretti J, Hasselmo ME. 2004. Ionic mechanisms in the generation of subthreshold oscillations and action potential clustering in entorhinal layer II stellate neurons. Hippocampus. 14(3), 368-84.

Fyhn M, Molden S, Witter MP, Moser EI, Moser MB. 2004. Spatial representation in the entorhinal cortex. Science. 305(5688), 1258-64.

Garden DL, Dodson PD, O'Donnell C, White MD, Nolan MF. 2008. Tuning of synaptic integration in the medial entorhinal cortex to the organization of grid cell firing fields. Neuron 60(5), 875-89.

Giocomo LM, Zilli EA, Fransen E, Hasselmo ME. (2007) Temporal frequency of subthreshold oscillations scales with entorhinal grid cell field spacing. *Science*. 315(5819):1719-1722.

Giocomo LM, Hasselmo ME. 2009. Knock-out of HCN1 subunit flattens dorsal-ventral frequency gradient of medial entorhinal neurons in adult mice. J Neurosci. 29(23), 7625-30.

Gray CM, Konig P, Engel AK, Singer W. 1989. Oscillatory responses in cat visual cortex exhibit inter-columnar synchronization which reflects global stimulus properties. Nature. 338: 334–337.

Gulyás AI, Megías M, Emri Z, Freund TF. 1999. Total number and ratio of excitatory and inhibitory synapses converging onto single interneurons of different types in the CA1 area of the rat hippocampus. J Neurosci. 19(22), 10082-97.

Hafting T, Fyhn M, Molden S, Moser MB, Moser EI. 2005. Microstructure of a spatial map in the entorhinal cortex. Nature. 436(7052), 801-6.

Harris NC, Constanti. 1995. A Mechanism of block by ZD 7288 of the hyperpolarization-activated inward rectifying current in guinea pig substantia nigra neurons in vitro. J Neurophysiol. 74(6), 2366-78.

Hasselmo ME. 2013. Neuronal rebound spiking, resonance frequency and theta cycle skipping may contribute to grid cell firing in medial entorhinal cortex. Philos Trans R Soc Lond B Biol Sci. 369(1635), 20120523.

Heys JG, Giocomo LM, Hasselmo ME. 2010. Cholinergic modulation of the resonance properties of stellate cells in layer II of medial entorhinal cortex. J Neurophysiol. 104(1), 258-70.

Heys JG, Hasselmo ME. 2012. Neuromodulation of I(h) in layer II medial entorhinal cortex stellate cells: a voltage-clamp study. J Neurosci. 32(26), 9066-72.

Hines ML, Carnevale NT. 1997. The NEURON simulation environment. Neural Comput. 9(6), 1179-209.

Hoffman DA, Magee JC, Colbert CM, Johnston D (1997) K+ channel regulation of signal propagation in dendrites of hippocampal pyramidal neurons. Nature. 387(6636):869-75.

Hutcheon B, Miura RM, Puil E. 1996. Subthreshold membrane resonance in neocortical neurons. J Neurophysiol. 76: 683–697.

Isaacson JS, Strowbridge BW. 1998. Olfactory reciprocal synapses: dendritic signaling in the CNS. Neuron. 20(4), 749-61.

Jahnsen H, Llinás R. 1984. Electrophysiological properties of guinea-pig thalamic neurones: an in vitro study. J Physiol. 349, 205-26.

Kasai M, Ono M, Ohmori H. 2012. Distinct neural firing mechanisms to tonal stimuli offset in the inferior colliculus of mice in vivo. Neurosci Res. 73(3):224-37.

King C, Reece M, O'Keefe J. 1998. The rhythmicity of cells of the medial septum/diagonal band of Broca in the awake freely moving rat: relationships with behaviour and hippocampal theta. Euro J Neurosci. 10:464–77.

Klink R, Alonso A. 1993. Ionic mechanisms for the subthreshold oscillations and differential electroresponsiveness of medial entorhinal cortex layer II neurons. J Neurophysiol. 70(1), 144-57.

Köhler C, Chan-Palay V, Wu JY. 1984. Septal neurons containing glutamic acid decarboxylase immunoreactivity project to the hippocampal region in the rat brain. Anat Embryol (Berl). 169(1):41-4.

Leung LS, Yu HW. 1998. Theta-frequency resonance in hippocampal CA1 neurons in vitro demonstrated by sinusoidal current injection. J Neurophysiol. 79(3), 1592-6.

Magee JC. 1998. Dendritic hyperpolarization-activated currents modify the integrative properties of hippocampal CA1 pyramidal neurons. J Neurosci. 18(19), 7613-24.

Magee JC, Cook EP. 2000. Somatic EPSP amplitude is independent of synapse location in hippocampal pyramidal neurons. Nat Neurosci. 3(9), 895-903.

Magee JC, Johnston D. 1995. Characterization of single voltage-gated Na+ and Ca2+ channels in apical dendrites of rat CA1 pyramidal neurons. J Physiol. 487 (Pt 1):67-90.

McCormick DA. 1998. Membrane properties and neurotransmitter actions. In: The Synaptic Organization of the Brain (edited by Shepherd GM. New York: Oxford), pp. 37–75.

McCormick DA, Bal T. 1997. Sleep and arousal: thalamocortical mechanisms. Annu Rev Neurosci. 20, 185-215.

Menon V, Musial TF, Liu A, Katz Y, Kath WL, Spruston N, Nicholson DA. 2013. Balanced synaptic impact via distance-dependent synapse distribution and complementary expression of AMPARs and NMDARs in hippocampal dendrites. Neuron. 80(6), 1451-63.

Micheva KD, Smith SJ. 2007. Array tomography: a new tool for imaging the molecular architecture and ultrastructure of neural circuits. Neuron. 55(1):25-36.

Migliore M, Ferrante M, Ascoli GA. 2005. Signal propagation in oblique dendrites of CA1 pyramidal cells. J Neurophysiol. 94(6), 4145-55.

Migliore M, Messineo L, Ferrante M. 2004. Dendritic Ih selectively blocks temporal summation of unsynchronized distal inputs in CA1 pyramidal neurons. J Comput Neurosci. 16(1), 5-13.

Miles R, Tóth K, Gulyás AI, Hájos N, Freund TF. 1996. Differences between somatic and dendritic inhibition in the hippocampus. Neuron. 16(4), 815-23.

Mizumori SJ, Ward KE, Lavoie AM. 1992. Medial septal modulation of entorhinal single unit activity in anesthetized and freely moving rats. Brain Res. 570(1-2):188-97.

Moser EI, Moser MB. 2008. A metric for space. Hippocampus. 18(12), 1142-56.

Pastoll H, Solanka L, van Rossum MC, Nolan MF. 2013. Feedback inhibition enables θ-nested γ oscillations and grid firing fields. Neuron. 77(1), 141-54.

Perez-Rosello T, Baker JL, Ferrante M, Iyengar S, Ascoli GA, Barrionuevo G. 2011. Passive and active shaping of unitary responses from associational/commissural and perforant path synapses in hippocampal CA3 pyramidal cells. J Comput Neurosci. 31(2), 159-82.

Person AL, Perkel DJ. 2005. Unitary IPSPs drive precise thalamic spiking in a circuit required for learning. Neuron. 46(1), 129-40.

Poolos NP, Migliore M, Johnston D. 2002. Pharmacological upregulation of h-channels reduces the excitability of pyramidal neuron dendrites. Nat Neurosci. 5(8), 767-74.

Quilichini P, Sirota A, Buzsaki G. 2010. Intrinsic circuit organization and theta-gamma oscillation dynamics in the entorhinal cortex of the rat. J Neurosci. 30:11128–42.

Schmidt-Hieber C, Häusser M. 2013. Cellular mechanisms of spatial navigation in the medial entorhinal cortex. Nat Neurosci. 16(3):325-31

Schreiber S, Erchova I, Heinemann U, Herz AV. 2004. Subthreshold resonance explains the frequency-dependent integration of periodic as well as random stimuli in the entorhinal cortex. J Neurophysiol. 92(1):408-15.

Shay CF, Boardman IS, James NM, Hasselmo ME. 2012. Voltage dependence of subthreshold resonance frequency in layer II of medial entorhinal cortex. Hippocampus. 22(8), 1733-49.

Shay CF, Ferrante M, Chapman GW, Hasselmo ME. 2015. Rebound Spiking in Layer II Medial Entorhinal Cortex Stellate Cells: Possible Mechanism of Grid Cell Function. Neurobiology of Learning and Memory. doi: 10.1016/j.nlm.2015.09.004.

Singer W, Gray CM. 1995. Visual feature integration and the temporal correlation hypothesis. Annu Rev Neurosci. 18: 555–586.

Steriade M. 1993. Central core modulation of spontaneous oscillations and sensory transmission in thalamocortical systems. Curr Opin Neurobiol. 3(4), 619-25.

Stuart G, Spruston N, Sakmann B, Häusser M. 1997. Action potential initiation and backpropagation in neurons of the mammalian CNS. Trends Neurosci. 20(3):125-31.

Tang Q, Burgalossi A, Ebbesen CL, Ray S, Naumann R, Schmidt H, Spicher D, Brecht M. 2014. Pyramidal and stellate cell specificity of grid and border representations in layer 2 of medial entorhinal cortex. Neuron. 84(6):1191-7.

Tsuno Y, Chapman GW, Hasselmo ME. 2015. Rebound spiking properties of mouse medial entorhinal cortex neurons in vivo. Eur J Neurosci. doi: 10.1111/ejn.13097.

Tsuno Y, Schultheiss NW, Hasselmo ME. 2013. In vivo cholinergic modulation of the cellular properties of medial entorhinal cortex neurons. J Physiol. 591(Pt 10), 2611-27.

van Welie I, van Hooft JA, Wadman WJ. 2004. Homeostatic scaling of neuronal excitability by synaptic modulation of somatic hyperpolarization-activated Ih channels. Proc Natl Acad Sci U S A. 101(14):5123-8.

Varela F, Lachaux JP, Rodriguez E, Martinerie J. 2001. The brainweb: phase synchronization and large-scale integration. Nat Rev Neurosci. 2(4):229-39.

Welday AC, Shlifer IG, Bloom ML, Zhang K, Blair HT. 2011. Cosine directional tuning of theta cell burst frequencies: evidence for spatial coding by oscillatory interference. J Neurosci. 31(45):16157-76.

Wessa P. 2012. Pearson Correlation (v1.0.6) in Free Statistics Software (v1.1.23-r7). Office for Research Development and Education (URL http://www.wessa.net/rwasp_correlation.wasp/).

Widmer H, Ferrigan L, Davies CH, Cobb SR. 2006. Evoked slow muscarinic acetylcholinergic synaptic potentials in rat hippocampal interneurons. Hippocampus. 16(7), 617-28.

Yokoi M, Mori K, Nakanishi S. 1995. Refinement of odor molecule tuning by dendrodendritic synaptic inhibition in the olfactory bulb. Proc Natl Acad Sci U S A. 92(8), 3371-5.

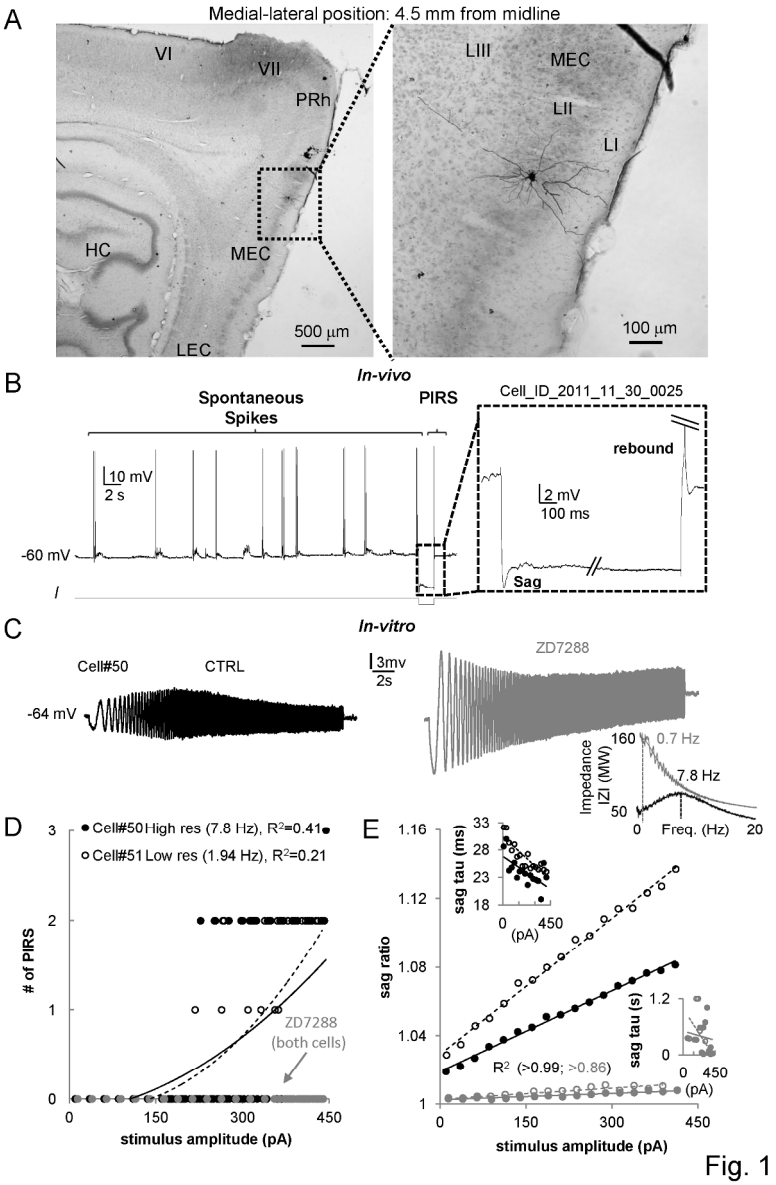

Fig. 1

190x279mm (300 x 300 DPI)

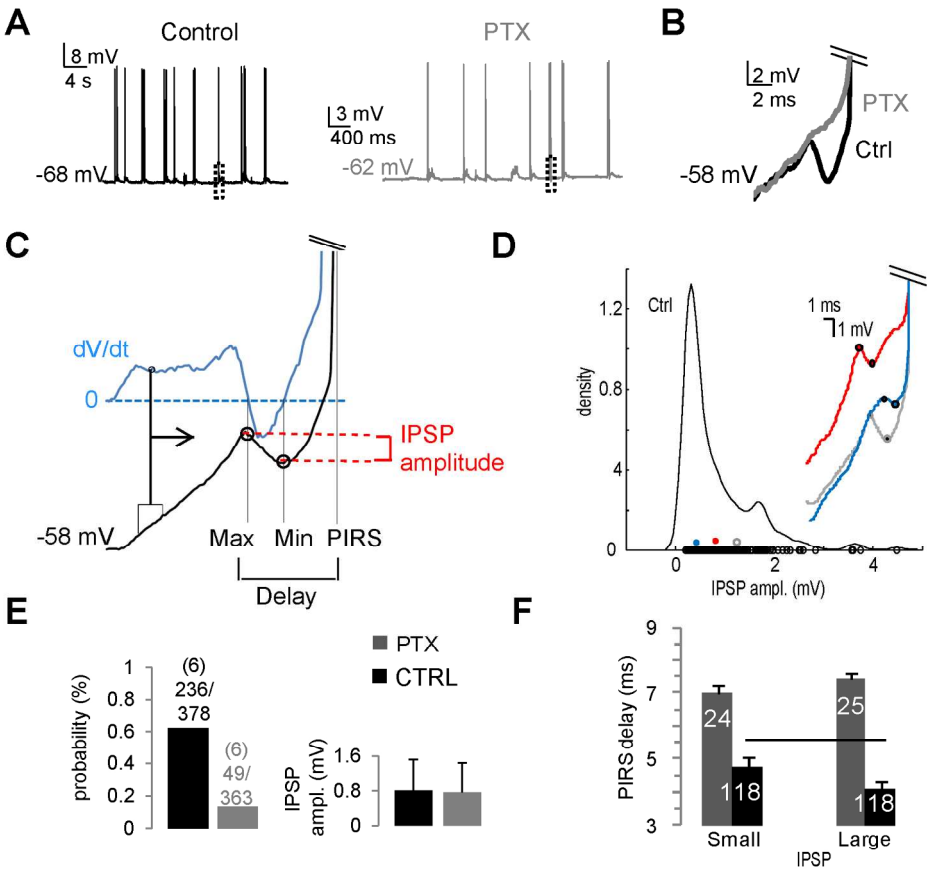

Fig. 2

176x177mm (299 x 299 DPI)

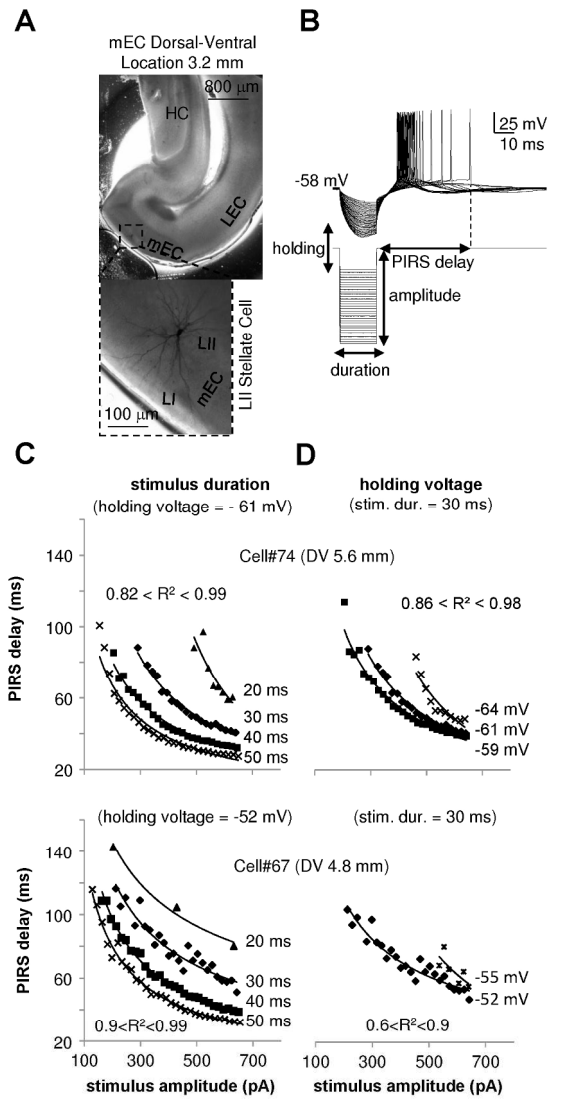

Fig. 3

120x254mm (300 x 300 DPI)

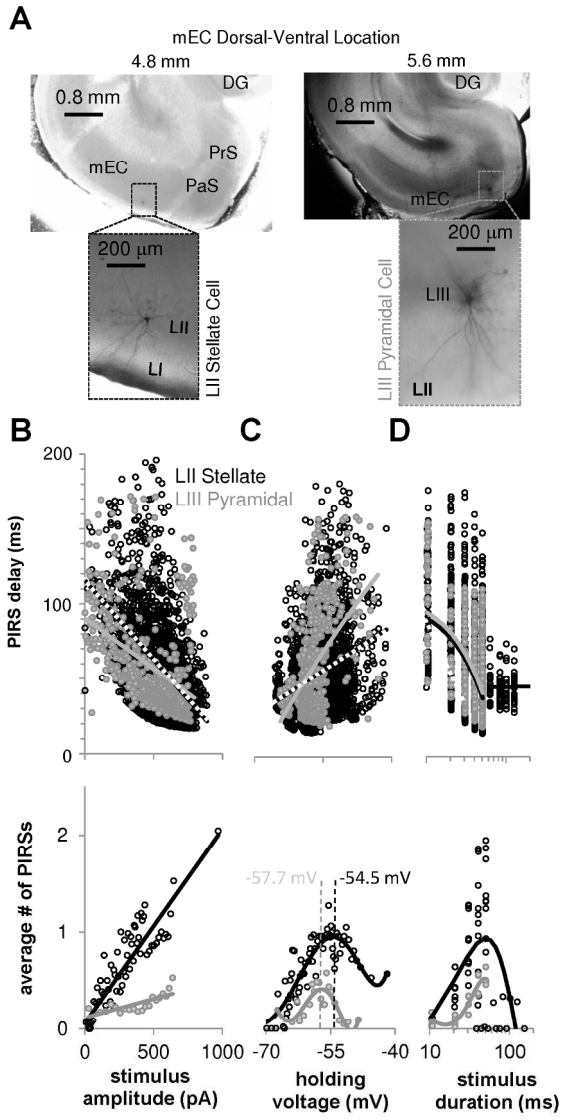

Fig. 4

120x239mm (300 x 300 DPI)

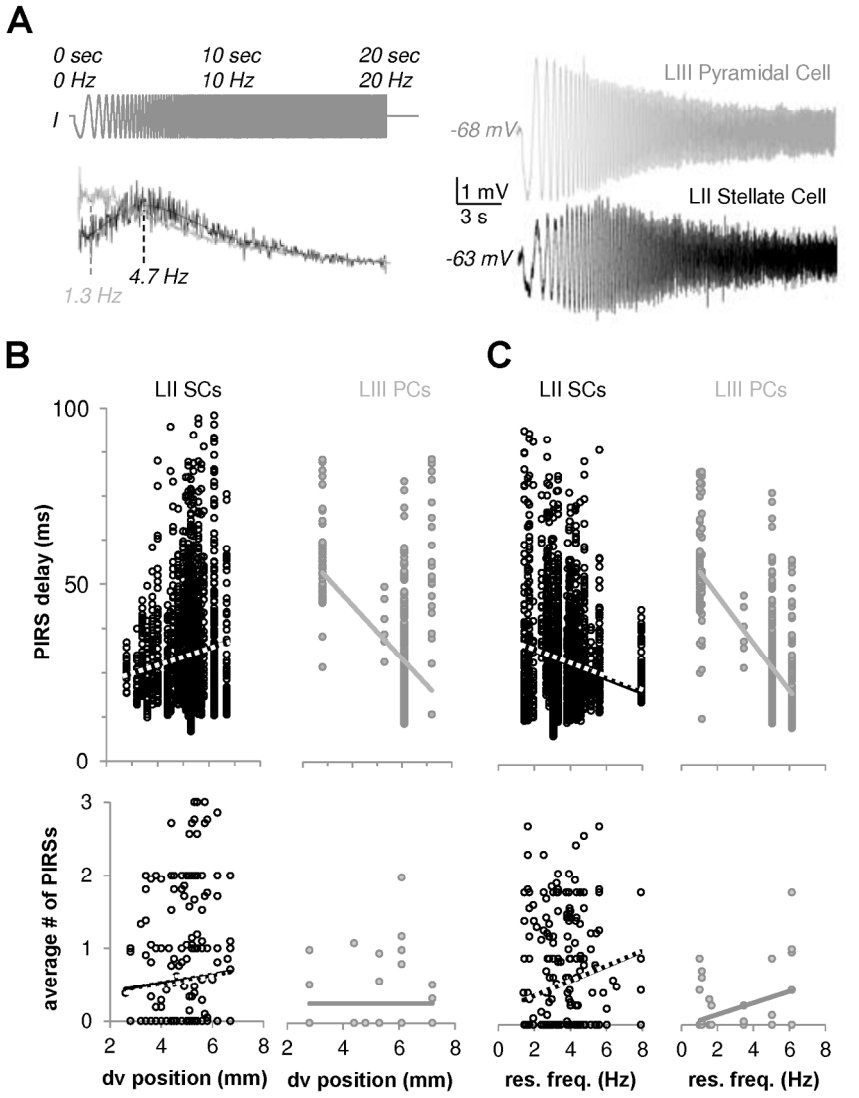

Fig. 5

155x205mm (300 x 300 DPI)

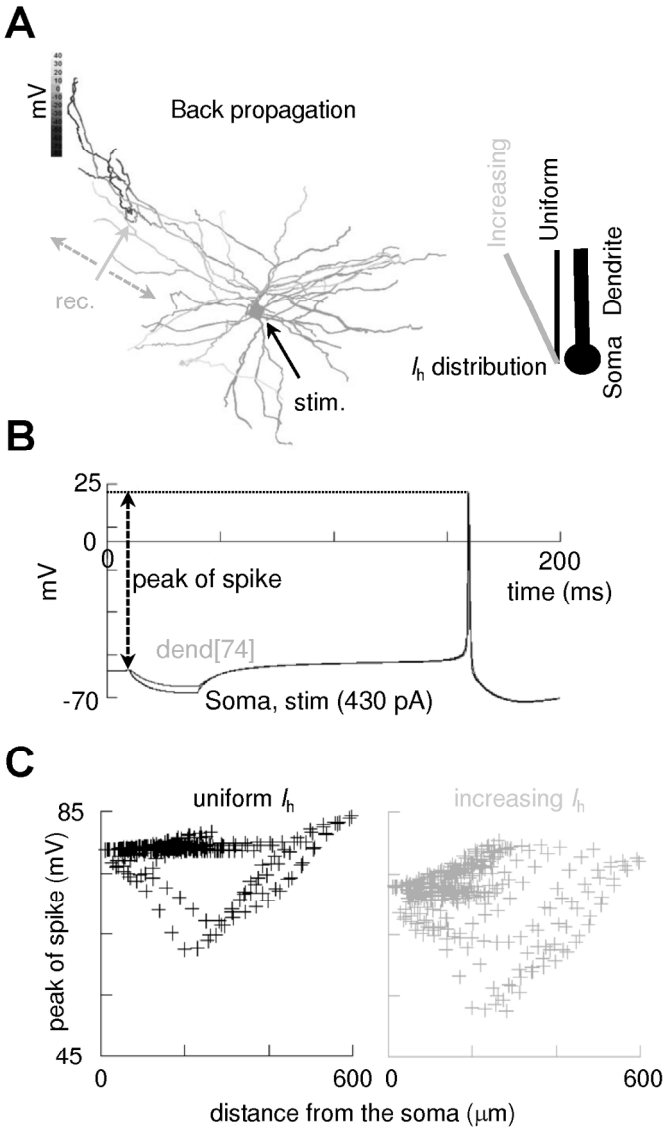

Fig. 6

98x175mm (300 x 300 DPI)

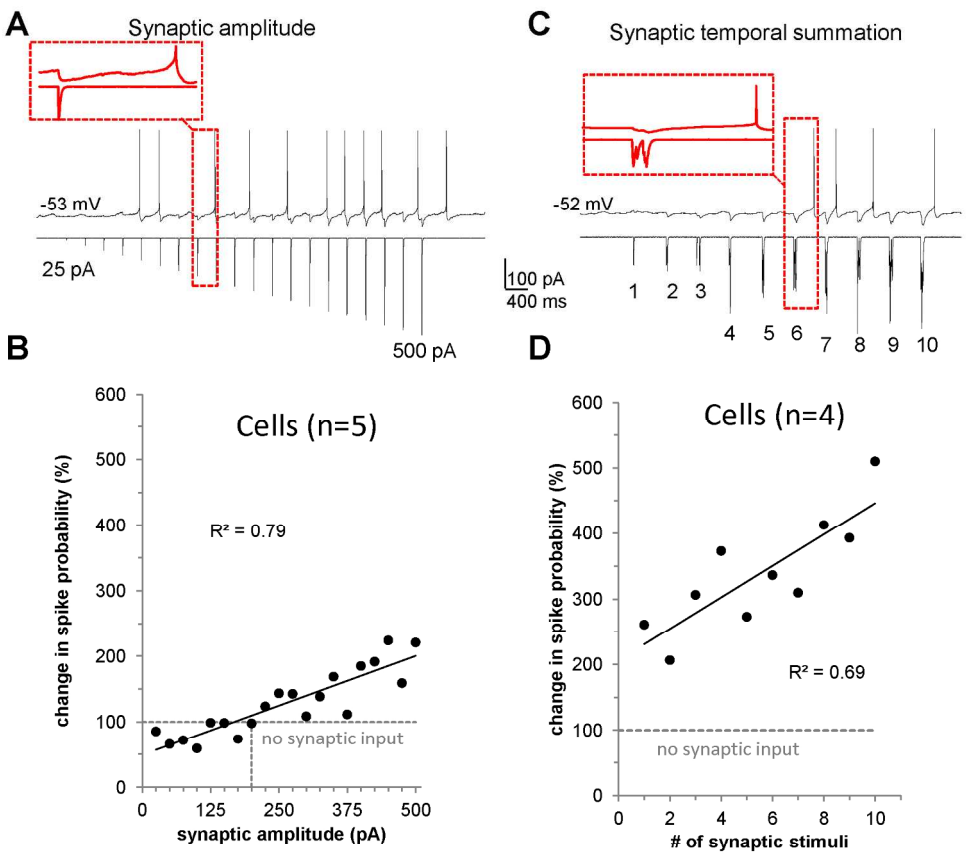

Fig. 7

190x181mm (300 x 300 DPI)

Post-Inhibitory Rebound Spikes in Rat Medial Entorhinal Layer II/III Principal Cells: *In-Vivo*, *In-Vitro*, and Computational Modeling Characterization

MICHELE FERRANTE,[1,2] CHRISTOPHER F SHAY,[1,2,3] YUSUKE TSUNO,[1,2] G WILLIAM CHAPMAN[1], and MICHAEL E HASSELMO[1,2,3]

[1] Center for Memory and Brain, Boston University, Boston, MA, 02215
[2] Department of Psychological and Brain Sciences, Boston University, Boston, MA, 02215
[3] Graduate Program for Neuroscience (GPN), Boston University, Boston, MA, 02215

Correspondence: Michele Ferrante, 2 Cummington Mall, Boston 02215, MA. Ph. 339-223-2340, mferr133@bu.edu

SUPPLEMENTAL FIGURE CAPTION

Supplemental Figure 1. *In-Vivo* Frequency–Current (f–I) curves suggest that inhibition makes mEC SCs more likely to fire an AP while reducing their average firing frequency. ***A***, *Bottom*, Current injected linearly increased from rest to 1000pA (upward ramp) and back to rest (downward ramp) in 90 seconds. *Top*, Voltage traces for control (in black) and picrotoxin (in gray), only voltage traces for upward ramps are shown. ***B***, Average amplitude of current injected necessary to elicit an AP for upward and downward ramps. Data are represented as mean ± SEM. Numbers in parentheses depict the number of cells recorded, while the numbers below represent the number of upward and downward ramp experiments run for each condition. ***C***, *Left*, Instantaneous firing frequency data for the ramp experiments in **A** fitted by logistic function I/O curves. *Right*, Instantaneous firing frequency of the cell population; calculated by averaging the logistic functions of all cells by condition. Inset shows the average number of spikes (n) for each trial (*i.e.,* on average 10.75 Hz and 21.52 Hz for control and picrotoxin conditions, respectively).

Supplemental Figure 2. *In-Vitro,* Single Cell Quantification of Stimulus-Dependent Changes in the Number of Post-Inhibitory Rebound Spikes. ***A***, Hyperpolarizing current stimulation protocol. The four currents and voltages traces depict a subthreshold signal (0), the threshold to elicit a single post-inhibitory rebound spike (1), a doublet (2), and a triplet (3). Holding current, stimulus duration, and amplitude were systematically changed to investigate their effect on the number of post-inhibitory rebound spikes. ***B***, *Left*, Effects of modulating stimulus amplitude (x-axis) and stimulus duration (different symbols) on the number of PIRS of two cells (*top* and *bottom*). *Right*, Effects of changing stimulus amplitude (x-axis) and holding voltage (different symbols) on the number of PIRS of two cells (*top* and *bottom*). These are 4 distinct SCs located between 5.1 and 5.6 mm on the mEC DV axis.

Supplemental Figure 3. *In-Vitro,* Depolarization Induced Spikes Are Faster but PIRS Are Generated by Smaller Inputs. ***A***, Depolarizing current stimulation protocol, highlighted are the current (bottom) and voltage (top) thresholds to generate a regular AP. Bars under the stimulus represent the time analyzed for stimulus durations of 10, 20, 30, 40, and 50 ms, from top to bottom. Total stimulation duration 500 ms. ***B***, AP delay as function of the depolarizing stimulus amplitude and the cellular holding voltage for two cells (left and right panel), to compare with Fig. 3*D*. Fitting lines are power functions. ***C***, Average number of APs as function of the depolarizing stimulus amplitude, for distinct stimulus durations (left) and holding voltages (right), to compare with Suppl. Fig. 2*B*. ***D***, Population response. Timing of the first spike (left) and average number of spikes (right) when the stimulus amplitude was manipulated. Regular APs shown in black, PIRS shown in gray. *Right,* The horizontal gray parenthesis depicts the stimulus range in which PIRS are more easily elicited than regular APs. Regular AP population results obtained from 77 cells performing 2167 depolarizing current step experiments. AP delays larger than 200 ms are not shown for

illustration purposes. Fitting lines on the left panel are power functions, fitting lines on the right panel are linear fits. To depict the full extent of the variability of the population response each panel shows the effect of one variable (*e.g.,* stimulus amplitude) when all the other variables (*e.g.,* holding voltage and stimulus duration) are independently manipulated.

Supplemental Figure 4. *In-Vitro,* Effect of Sag Ratio and Sag Time Constant (tau) on PIRS Properties of mEC-LII-SCs and mEC-LII/III-PCs. ***A***, Representative differences in the voltage response of a mEC-LII-SC (black) and a mEC-LII/III-PC (gray) to the same hyperpolarizing current injection. ***B***, Left, Sag ratio as function of the stimulus amplitude for SCs (black, n = 1528, R = 0.799, $p < 0.01$) and PCs (gray, n = 198, R = 0.288, $p < 0.01$). Center and right, sag tau as function of the stimulus amplitude, for SCs (n = 1484, R = -0.077, $p < 0.01$) and PCs (n = 187, R = 0.186, $p < 0.02$) respectively. Y-axes are in log scale. ***C***, Sag ratio effect on PIRS delay (Top) and average number of PIRS (Bottom) for the two mEC cell classes. Top panel, SCs (n = 991, R = -0.311, $p < 0.01$); PCs (n = 47, R = 0.1, p = 0.25); bottom panel SCs (n = 2689, R = 0.335, $p < 0.01$) PCs (n = 31, R = -0.183, p = 0.16). ***D***, Impact of sag tau on PIRS delay (Top) and average number of PIRS (Bottom) for the two mEC cell classes. Top panel, SCs (n = 961, R = 0.2, $p < 0.01$); PCs (n = 25, R = 0.486, $p < 0.01$); bottom panel SCs (n = 233, R = -0.685, $p < 0.01$) PCs (n = 24, R = -0.79, p = 0.01). Tau values larger than 60 ms were not potted.

Supplemental Figure 5. Simulations, Experimental Validation of the Computational Model. ***A***, 3D reconstruction of a mEC LII Stellate Cell (coming from the Nolan lab downloaded from Neuromorpho.org). Gray scale depicts dendritic invasion of a PIRS generated somatically, as in the experiments (*e.g.,* Figure 1A-B). ***B***, Model voltage response to a ZAP stimulus (amplitude 100pA) in control condition (top) and with I_h blocked (bottom), compare with experiments in Figure 1C. ***C***, Impedance plot showing peak resonant frequencies for the two traces in B. ***D***, PIRS timing as a function of the stimulus amplitude to compare with experiments in Figure 3B. Sub-threshold input amplitude is 400pA at maximum (for 30 ms). For each subsequent sweep the stimulus amplitude was increased by either 25 or 33 pA, as in the experiments. Inset, depicts absence of PIRS when I_h was blocked, as in the experiments (Figure 1D). ***E***, Computational model (black) matching the experimental (gray) relationship between stimulus amplitude and PIRS delay for all the stimulus durations (20, 30, 40, and 50 ms). ***F***, Subsample, 3 of the 22 realistic neuronal morphologies (coming from the Nolan Lab, downloaded from Neuromorpho.org) organized according to their mEC DV location. I_h kinetic properties were also varied along the DV according to previous experimental data recorded in our lab (Giocomo and Hasselmo, 2008). Be aware that the DV location in these morphologies is calculated, as in the original manuscript, from the dorso-caudal pole of the mEC and differs from our method that calculates it from dorsal surface of the brain (adding 2-2.5 mm to the former measurement). ***G***, Resonant response of the most dorsal cell (0.5 mm, 7.17 Hz resonance frequency) compared with the most ventral cell (5.5 mm 3.9 Hz resonance frequency). Note the difference on y-axis scales for the two insets.

Supplemental Figure 6. Simulations, mEC DV differences in I_h kinetic properties and neuronal morphologies have opposite effects on the spike timing. Experimental differences in the I_h fast and slow kinetics along the DV axis of the mEC have been implemented in the model (see methods). Black symbols show the effect on PIRS delay of changing DV I_h kinetics on a single neuronal morphology. Similarly, with the gray symbols, we investigated the role of neuronal morphology on PIRS delay by using different neuronal morphologies collected along the DV axis of the mEC (see methods) and applying a fixed set I_h DV kinetics for all of them.

Supplemental Figure 7. Simulations, Effects of I_h Dendritic Distribution on PIRS Generation and Forward Propagation. ***A***, Schematic of the forward propagation protocol. For each simulation the position of the stimulating electrode was changed to determine the stimulus amplitude and voltage threshold (v_thresh) necessary to elicit a PIRS. ***B***, Voltage response for the locally generated (in a distal branch) and forward propagated (to the soma) PIRS. ***C***, Stimulus amplitude effect on the percentage of dendritic

branches generating PIRS, for uniform (black) and increasing (gray) distribution of I_h. ***D***, Voltage threshold necessary to elicit PIRS in a given percentage of dendritic branches, for uniform (black) and increasing (gray) distribution of I_h. Dashed lines represent the effect of the full activation of $GABA_A$ (Erev = -70 mV) and $GABA_B$ (Erev = -95 mV) receptors on the percentage of branches firing PIRS.

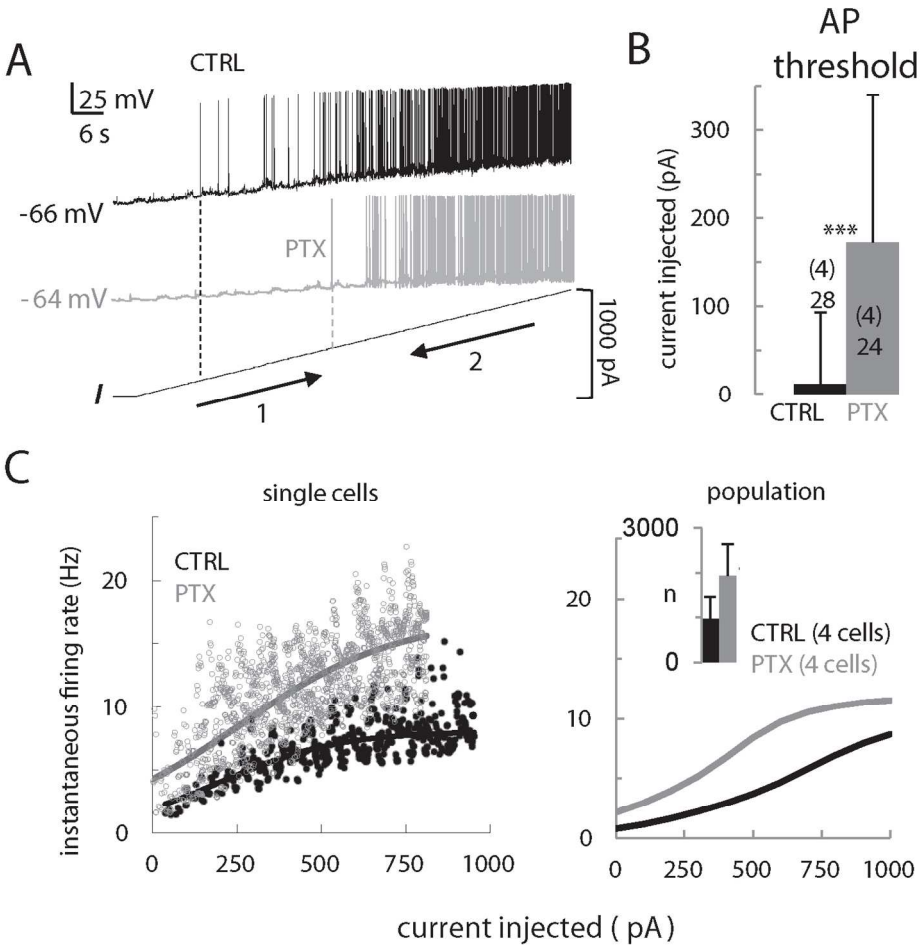

Suppl. Fig. 1

136x152mm (300 x 300 DPI)

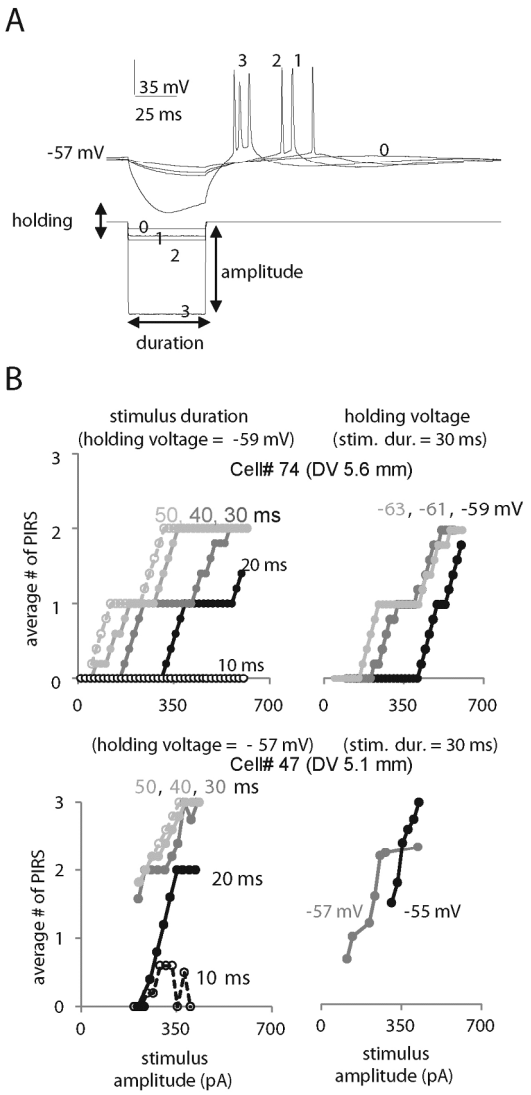

Suppl. Fig. 2

104x222mm (300 x 300 DPI)

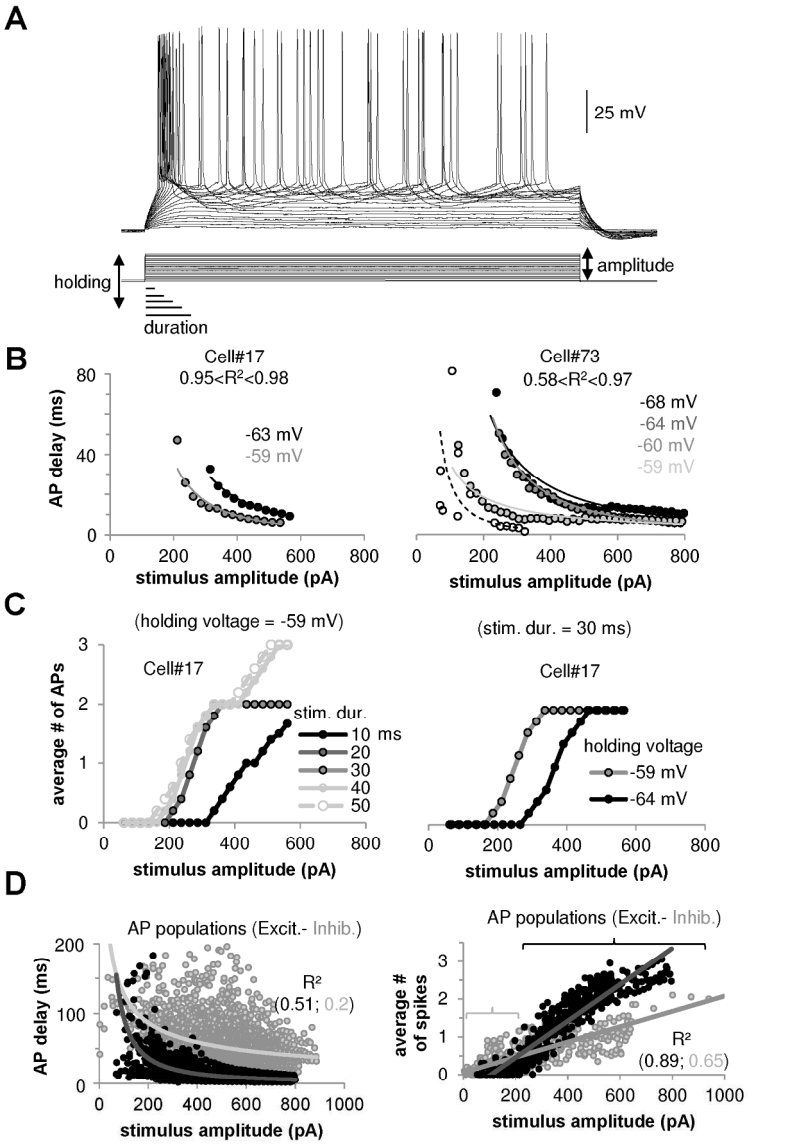

Suppl. Fig. 3

161x236mm (300 x 300 DPI)

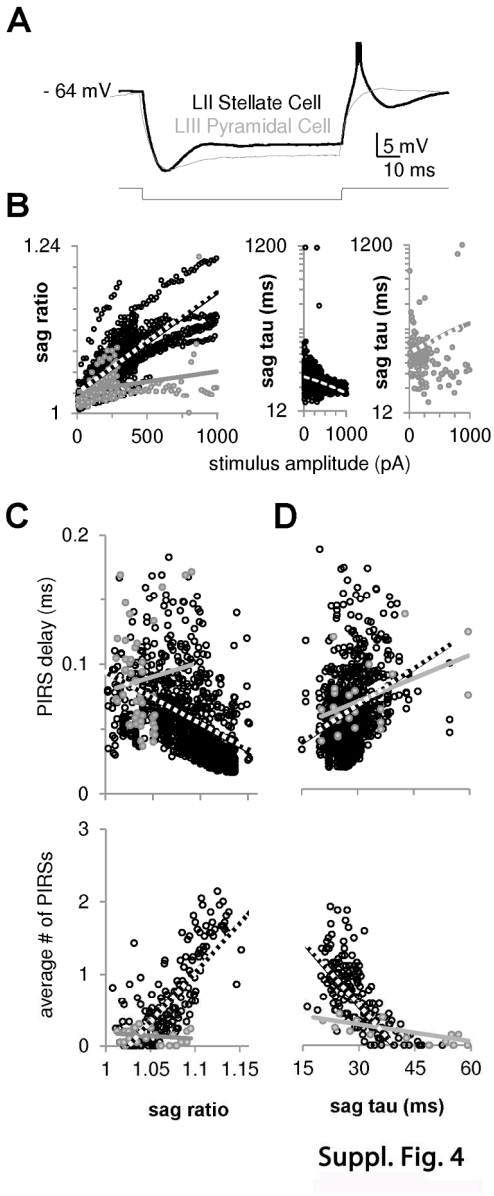

Suppl. Fig. 4

94x218mm (300 x 300 DPI)

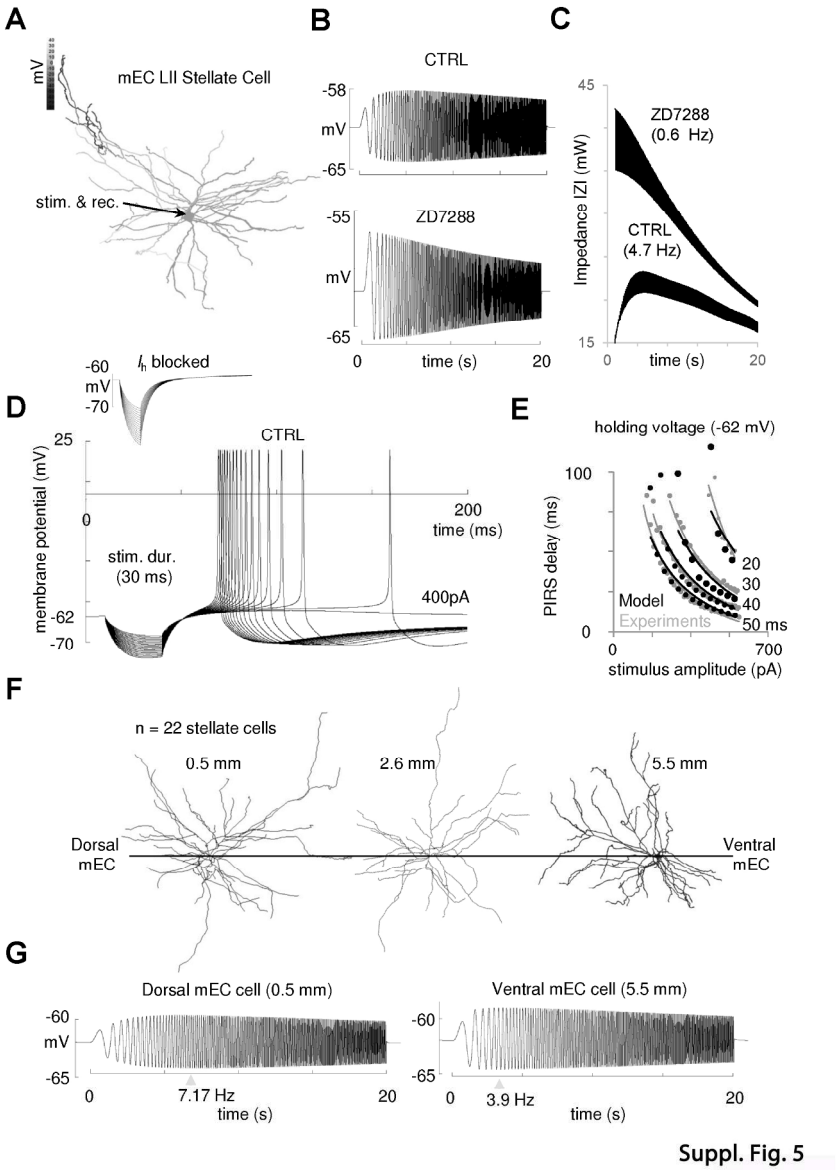

Suppl. Fig. 5

190x254mm (300 x 300 DPI)

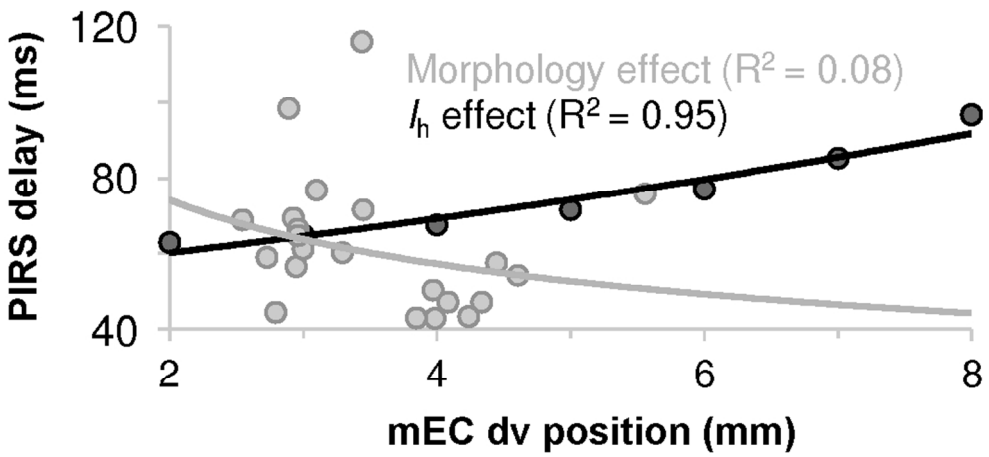

Suppl. Fig. 6

91x51mm (300 x 300 DPI)

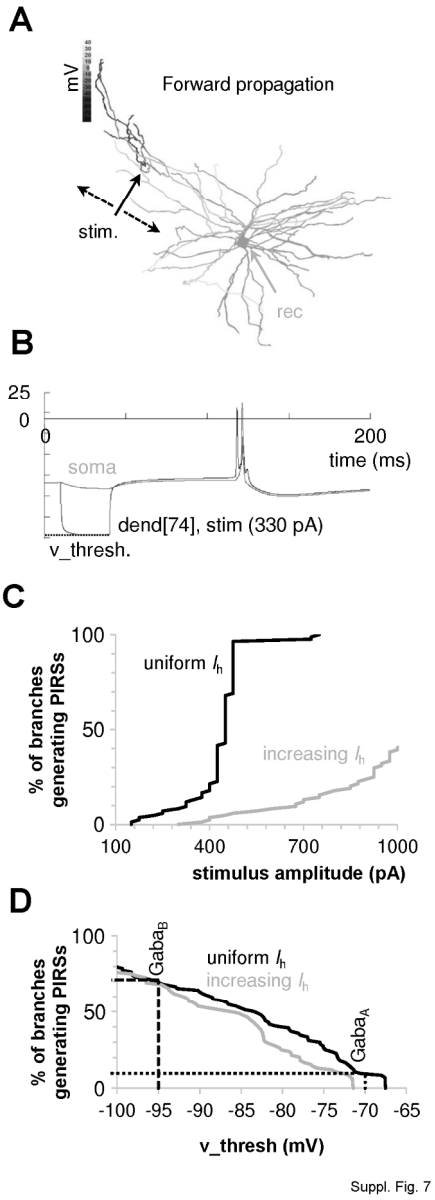

Suppl. Fig. 7

84x224mm (300 x 300 DPI)